New SMOS Sea Surface Salinity with reduced systematic errors and improved variability

Jacqueline Boutin, Jean-Luc Vergely, Stéphane Marchand, Francesco d'Amico, Audrey Hasson, Nicolas N. Kolodziejczyk, Nicolas Reul, Gilles Reverdin, Jérôme Vialard

New SMOS Sea Surface Salinity with reduced systematic errors and improved variability

J. Boutin[(1)], J.L. Vergely[(2)], S. Marchand[(1)], F. D'Amico[(1)], A. Hasson[(1)], N. Kolodziejczyk[(3)], N. Reul[(3)], G. Reverdin[(1)], J. Vialard[(1)]

[(1)] Sorbonne Université, CNRS, IRD, MNHN, Laboratoire d'océanographie et du climat : expérimentations et approches numériques (LOCEAN), 75005 Paris, France

[(2)] ACRI-st, Guyancourt, France

[(3)] LOPS, CNRS/UBO/Ifremer/IRD, Plouzané/Toulon, France

Highlights:

1. Improved SMOS salinity systematic error correction from Kolodziejczyk et al. (2016).
2. Refined variability of surface salinity near e.g. major river mouths.
3. Consistent mesoscale patterns observed by SMOS and SMAP satellite missions.

Corresponding author: Dr. Jacqueline Boutin, E-mail: jb@locean-ipsl.upmc.fr

Abstract

Salinity observing satellites have the potential to monitor river fresh-water plumes mesoscale spatio-temporal variations better than any other observing system. In the case of the Soil Moisture and Ocean Salinity (SMOS) satellite mission, this capacity was hampered due to the contamination of SMOS data processing by strong land-sea emissivity contrasts. Kolodziejczyk et al. (2016) (hereafter K2016) developed a methodology to mitigate SMOS systematic errors in the vicinity of continents, that greatly improved the quality of the SMOS Sea Surface Salinity (SSS). Here, we find that SSS variability, however, often remained underestimated, such as near major river mouths. We revise the K2016 methodology with: a) a less stringent filtering of measurements in regions with high SSS natural variability (inferred from SMOS measurements) and b) a correction for seasonally-varying latitudinal systematic errors. With this new mitigation, SMOS SSS becomes more consistent with the independent SMAP SSS close to land, for instance capturing consistent spatio-temporal variations of low salinity waters in the Bay of Bengal and Gulf of Mexico. The standard deviation of the differences between SMOS and SMAP weekly SSS is less than 0.3 pss in most of the open ocean. The standard deviation of the differences between 18-day SMOS SSS and 100-km averaged ship SSS is 0.20 pss (0.24 pss before correction) in the open ocean. Even if this standard deviation of the differences increases closer to land, the larger SSS variability yields a more favorable signal-to-noise ratio, with r^2 between SMOS and SMAP SSS larger than 0.8. The correction also reduces systematic biases associated with man-made Radio Frequency Interferences (RFI), although SMOS remains more impacted by RFI than SMAP. This newly-processed dataset will allow the analysis of SSS variability over a larger than 8 years period in regions previously heavily influenced by land-sea contamination, such as the Bay of Bengal or the Gulf of Mexico.

1. Introduction

With 8 years and counting, the Soil Moisture and Ocean Salinity (SMOS) European mission (Kerr et al., 2010; Font et al., 2010) provides the longest record for Sea Surface Salinity (SSS[a]) monitored from space over the global ocean (2010-present). The pioneered SMOS (2010-) and Aquarius (2011-2015) (Largeloef, 2008) satellite missions have demonstrated the capability of L-band radiometry for monitoring SSS from space (e.g. Reul et al., 2014a; Lagerloef, 2012).

Salinity is a key ocean variable that plays a fundamental role in the density-driven global ocean circulation, the water cycle, and climate (Siedler et al., 2001). Salinity controls the density of sea water, together with temperature. At the ocean surface, in cold waters (T = 2 °C), a SSS change of ~0.1 pss[b] is equivalent, in terms of density, to a sea surface temperature (SST) change of 1°C. SSS variations therefore greatly constrain the global thermohaline circulation as salinity drives the high latitude convective overturning. In warmer regions (T=28 °C), a 0.44 pss change is equivalent to a 1 °C change in terms of density. Salinity stratification within a near isothermal layer (known as the barrier layer, e.g. Lukas and Lindstrom, 1991) can furthermore inhibit the vertical mixing of heat and momentum, and play a role in major phenomena such as the El Niño Southern Oscillation (e.g. Vialard and Delecluse, 1998), the southwest monsoon rain distribution (e.g. Shenoi et al. 2002) or the oceanic productivity (e.g. Picaut et al. 2001). Finally, SSS is considered as a passive tracer of

[a] SSS will hereafter refer to the salinity measured between 1 cm -as monitored by satellite measurements- and at a few meters depth -as monitored by most *in situ* measurements.
[b] pss is used here as an equivalent to gram of salt per kilogram of standard sea water, see UNESCO (1985) for more details

63 the hydrological cycle, recording for instance its intensification in response to anthropogenic
64 climate change (e.g. Durack et al. 2012). For all these reasons, SSS has been designated as an
65 ECV (Essential Climate Variable) by the Global Climate Observing System (GCOS).

66 SMOS data has enabled the study of salinity changes associated with two El Niño events
67 (Hasson et al. submitted) and a La Niña event (Hasson et al. 2014), climate variability in the
68 equatorial Indian Ocean (Durand et al. 2013), decadal salinity changes in the subtropical
69 Pacific Ocean (Hasson et al. 2013) or North Atlantic Ocean (Grodsky et al. 2017). The spatial
70 resolution and spatio-temporal coverage of the SMOS mission (50 km resolution; global
71 coverage every 3 to 5 days) also allow the unprecedented detection of SSS mesoscale features
72 associated with the transport across frontal regions (e.g. Reul et al., 2014b; Kolodziejczyk et
73 al., 2015), very hardly accessible from Aquarius measurement (100-150 km resolution; global
74 coverage every 8 days).

75 SMOS demonstrated performance in monitoring open-ocean salinity variations has been
76 impressive so far. SMOS results have, however, been disappointing close to land, for instance
77 in the Bay of Bengal, where Aquarius and more recently the Soil Moisture Active Passive
78 (SMAP; 2015-) mission perform better (Akhil et al. 2016 and Fournier et al. 2017).

79 SMOS is an Earth Explorer mission. It carries an L-band Microwave Interferometric
80 Radiometer with Aperture Synthesis (MIRAS), which is the first interferometer and the first
81 L-band radiometer observing Earth from space. L-band (1.4 GHz) is a passive protected
82 frequency band but many SMOS measurements are corrupted by unexpected man-made
83 Radio Frequency Interferences (RFI) (Oliva et al., 2012). SMOS SSS is also affected by the
84 presence of nearby landmasses up to several hundreds of kilometers into the ocean, likely an
85 effect of imperfect synthetic aperture image reconstruction in the present SMOS data

processing (more on limitations in the present SMOS image reconstruction is presented in Anterrieu et al., 2015).

Other two satellite missions measuring SSS from space, Aquarius (Lagerloef et al., 2008) (2011-2015) and SMAP (Piepmeier et al., 2017) (2015-present), are equipped with classical L-band radiometers. Hence, they are expected to suffer less land-sea contamination than SMOS. Aquarius and SMAP were launched subsequently to SMOS and have benefited from a better RFI-protected onboard processing.

The unique length of SMOS record and its high spatio-temporal resolution (comparable to the more recent SMAP mission) are strong motivations for improving its processing in order to mitigate RFI and land-sea contaminations on the retrieved SSS. The validation of satellite SSS using *in situ* SSS measurements is, however, very challenging in coastal areas where contaminations are strong, in situ data are very sparse and variability is high, such as in river plumes (Delcroix et al. 2005; Boutin et al. 2016). Hence, in addition to using *in situ* SSS, we take advantage of SMAP SSS to assess corrections to the SMOS SSS.

Kolodziejczyk et al. (2016) (K2016 hereafter) have developed a Bayesian methodology to mitigate SSS systematic errors due to land-sea contamination. The method is described in detail in Section 3.3 of the present paper. It brings a clear improvement in most areas, with a 32% decrease of the RMSD globally with respect to ship measurements. Some examples below, however, indicate much lower SSS values in SMAP than in K2016 SMOS retrievals, in particular near river mouths. In the Bay of Bengal, for instance, fresh water originating from the Ganges-Brahmaputra (GB) is transported southward by the East India Coastal Current (EICC) after the monsoon, forming a ~200 km fresh water tongue along the Indian coast, up to 10 pss fresher than in the central Bay of Bengal (Chaitanya et al. 2014). Fournier

et al. (2017) demonstrated the SMAP capacity to monitor the modulation of this freshwater tongue extent by climate variability and mesoscale eddies stirring the freshwater plume away from the coast. This peculiar pattern is more than 3 pss fresher in SMAP SSS than SMOS K2016 SSS (Figure 1 a and c). Fournier et al. (2016) similarly used SMAP data to study an unusual freshening associated with anomalous advection of the Mississippi River plume in the Gulf of Mexico. While this freshening is also detected by SMOS K2016 (Figure 1 d), it is saltier than in SMAP SSS (Figure 1 f). Such overestimation of K2016 SSS by SMAP relative to SMOS in the low salinity regime also occurs in the eastern tropical Atlantic (Figure 1 g, i, Congo and Niger river mouths, Reul et al. 2014a) and western tropical Atlantic (Amazon and Orinoco, Figure 1 j, l). SMOS K2016 default in retrieving the freshest SSS of the major river plumes illustrates the need of an improved processing in variable, low-salinity regions near land.

The purpose of this paper is to present a revised version of the K2016 methodology. The main changes aim at taking the SSS natural variability into consideration in the land-sea contamination correction and at adding a correction for the seasonally-varying latitudinal biases.

Ancillary datasets are detailed in section II. An overview of the SMOS SSS retrieval, of the K2016 SMOS processing and a description of the revised methodology are given in section III. Comparisons with ancillary data sets are presented in section IV and V. They are summarized and discussed in section VI.

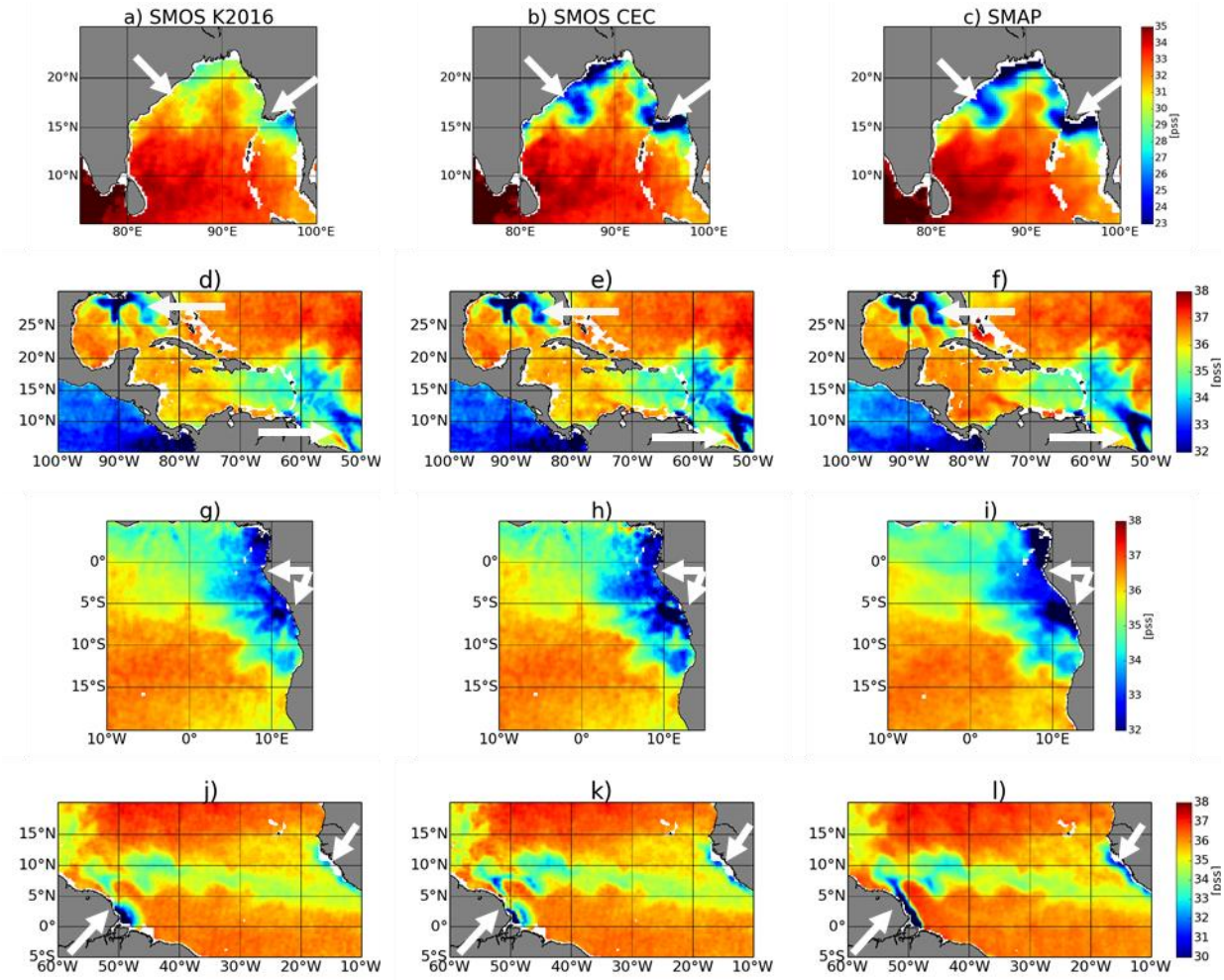

Figure 1: Satellite SSS: SMOS SSS corrected according to (a, d, g, j) K2016 methodology, (b, e, h, k) the method described in this paper (CEC); (c, f, i, l) SMAP SSS. 4 case study areas : (a, b, c) : Bay of Bengal - August 21st 2015; (d, e, f) : Gulf of Mexico – August18th 2015 ; (g, h, i) : Eastern Tropical Atlantic Freshwater Pools – April 14th 2016; (j, k, l) : Amazon plume – October 21st 2015. SMOS and SMAP SSS is averaged over a SMOS repetitive orbit sub-cycle (18 days) and two SMAP repetitive orbit cycles (16 days) respectively. Striking fresh SSS features in better agreement with SMOS (new version) and SMAP are indicated with white arrows.

2. Data

Three types of ancillary data are used in this study. The *In situ* Analysis System (ISAS) SSS is used both to set the long term mean reference of our correction and to qualitatively indicate the most trustable SMOS SSS data in our correction process as described in Section 3. It is

also used to check the SMOS SSS variability. SMAP and ship SSS are used for independent assessment.

2.1 *In Situ* Analyzed SSS

Monthly gridded fields of salinity derived from *in situ* measurements are obtained from the ISAS (*In situ* Analysis System) v6 algorithm, an optimal interpolation (Bretherton, 1976) tool developed for the synthesis of the Argo global dataset (Gaillard et al., 2016). We use the fields reconstructed at 5 m depth on a half degree horizontal grid. The ISAS Near Real Time (NRT) products are available since 2010. In addition, over the 2002-2012 period, ISAS13 (Gaillard, 2015) fields have been produced after a refined quality check of the Argo profiles. Data are preprocessed for ISAS13 using a climatological test and followed by a visual control of suspicious profiles. The interpolation is based on delayed mode Argo floats, TAO-TRITON-PIRATA-RAMA moorings and MEMO (Marine Mammals) data.

The ISAS-NRT fields (2010-present) are used by the correction method whereas ISAS13 (till 2012) and ISAS-NRT (from 2013 to 2016) fields are used for the assessment presented Section 4.

2.2 SMAP SSS

The SMAP mission (Piepmeier et al. 2017) provides L-band radiometric observations since April 2015. While its main objective is the observation of soil moisture, the observed brightness temperatures (Tb) are also used to retrieve SSS (Fore et al. 2016a). SMAP SSS characteristics are quite close to those of SMOS in terms of spatio-temporal coverage and spatial resolution (~50 km). In approximately 3 days, SMAP achieves global coverage and it has an exact orbit repeat cycle of 8 days. The SMAP L-band microwave radiometer, however, uses a conical scanning antenna instead of a synthetic aperture imaging antenna. As

stated in the introduction, a particular attention was put on filtering the RFI (Mohammed et al. 2016) and their impact is expected to be limited compared to SMOS. SMAP also suffers from land-sea contamination but, given that SMAP carries a real aperture antenna, the contamination is not expected to be as spatially variable as with SMOS. We use level 3 SMAP SSS produced at the Jet Propulsion Laboratory using the Combined Active Passive (CAP version 3) algorithm (Fore et al. 2016b). A complete description of the CAP v3 algorithm can be found in Fore et al. (2016a), but a brief description follows. The CAP algorithm is only applied to passive measurement as the radar failed a few months after launch. It includes specific Tb corrections for land and galactic noise contaminations, and a global Tb bias adjustment (latitude and time-dependent). After correction, the rms difference of SMAP retrieved SSS with respect to Hycom SSS in the vicinity to land is less than 1.5pss. Level 2 SSS is retrieved from SMAP Tb measurements using a constrained objective function minimization. Data are mapped on a 0.25° grid using a Gaussian weighting with a search radius of approximatively 45 km and a half-power radius of 30 km. They are aggregated in level 3 maps produced daily with an 8-day running-average time window. CAPv3 SMAP SSS agrees well with in situ SSS. Tang et al. 2017 found a rms difference of 0.26 pss between weekly SMAP SSS and buoy SSS. They also show that SMAP and SMOS SSS depict salinity fluctuations very close to in situ SSS.

2.3 Ship SSS

Salinity data provided by thermosalinographs (TSG) installed on voluntary merchant ships are used as ground truth. A full description of the data can be found in Alory et al. (2015). They provide SSS estimates with an ~2.5 km resolution along the ship track and are independent from the ISAS analyses. Samples are taken at a few meters depth. Noise on individual ship SSS is estimated to be on the order of 0.08 pss (Alory et al. 2015). In the

presence of strong vertical stratification, TSG and satellite SSS are expected to differ as the L-band radiometer skin depth is about 1 cm (Boutin et al. 2016). This may occur under heavy rain conditions or in river plumes. Because of their singular spatio-temporal resolution, ship measurements, however, provide invaluable information on the spatial variability of SSS unresolved by Argo.

3. SMOS data and processing methodology

The SMOS mission (Kerr et al., 2010) provides SSS measurements from space since January 2010. The SMOS satellite is on a sun-synchronous circular orbit with a local equator-crossing time at 6 AM on the ascending node and with a repeat sub-cycle of 18 days. It carries a 2-D interferometric radiometer, the MIRAS instrument. This groundbreaking technology was chosen as it involves much lighter antennas than real aperture antennas, and while getting ground spatial resolution on the order of 50 km at L-band frequency requires a huge antenna. The synthetic aperture antenna approach involves the reconstruction of an image using spatial Fourier components as derived from the correlations between numerous antenna elements (69 in case of SMOS). The SMOS bi-dimensional multi-angular images of Tb are reconstructed with a spatial resolution in the field of view ranging between about 35 km and 100 km (50 km on average). In this paper, we use the SSS retrieved within the center part of the field of view that extends at +/-400 km away from the center of the satellite swath. Global ocean coverage is then achieved after about 5 days. Individual Tbs are very noisy (1.6-3.2 K) and lead to a typical noise on SSS of the order of 0.6 pss in tropical and subtropical regions on pixel-wise SSS retrievals (Hernandez et al., 2015; Supply et al., 2017). However, owing to the very good spatio-temporal coverage of SMOS, averaging SMOS SSS over typically one month and 100x100 km^2 results in an accuracy close to 0.2 pss in the open ocean, after removing a climatological mean of SMOS systematic errors (Boutin et al., 2016).

In the following, before describing the new SSS correction methodology developed in the present paper, we recall in section 3.1, the principle of the along track (level 2, L2) SMOS SSS retrieval from Tb measurements, and, in section 3.2, the basis for the K2016 correction method applied to L2 SSS.

3.1 SMOS SSS level 2 retrieval

The SMOS L2 SSS is retrieved from Level 1 (L1) Tb through a maximum-likelihood Bayesian approach in which Tb measured in the antenna reference frame, Tb^{meas}, are compared with Tb simulated using a forward radiative transfer model, Tb^{mod} (see a general description of the retrieval algorithm in Zine et al. (2008)). The retrieved parameters, P_i, and their associated theoretical error, are estimated through the minimization of the χ^2 cost function:

$$\chi^2 = \sum_{n=1}^{N} \frac{[Tb_n^{meas} - Tb_n^{mod}(\theta_n, P_i \ldots)]^2}{\sigma_{Tbn}^2} + \sum_{n=1}^{M} \frac{[P_i - P_{i0}]^2}{\sigma_{Pi0}^2}, \qquad (1)$$

where N is the number of measurements available for retrievals in vertical and horizontal polarizations at different incidence angles θ_n. N is typically 120 to 240 within +/-400 km from the center of the track. σ_{An} is taken equal to the SMOS brightness temperature noise (between 1.6 and 3.2K depending on the location within the field of view) plus a small term that takes into account an error originating from the radiative transfer model error (see Zine et al. 2008 for more details). M is the number of physical parameters, P_i (SSS, wind, sea surface temperature and ionospheric total electronic content) that are adjusted by the retrieval; P_{i0} and σ_{Pi0} are a priori values for P_i and their associated errors respectively.

In the present study, we use SSS produced at the Data Production Center (CPDC) of the Centre Aval de Traitement des Données SMOS (CATDS) in its RE05 version (Vergely and

Boutin, 2017). Daily SSS fields are provided on a 25-km resolution EASE 2 (Equal-Area Scalable Earth 2) grid (Brodzik et al. 2012) for ascending and descending orbits separately (CATDS, 2017a). L1 Tbs, radiative transfer models (roughness model 1) and retrieval scheme used in CATDS CPDC RE05 are identical to the ones used in the European Space Agency level 2 ocean salinity processor version 622 (ESA L2OS v622) (see a description in SMOS-Ocean Expert Support Laboratories (2014)). The main difference between the CATDS RE05 and the ESA v622 processing involves the Tb outlier filtering. No Tb outlier filtering is applied when retrieving SSS with ESA L2 OS V622. The absence of Tb outlier filtering enables an easier detection of RFI-polluted SSS through a larger χ^2 value (equation 1). This, however, removes pixels that are systematically contaminated by the presence of nearby land, which could be mitigated by our correction. K2016 correction method was indeed developed using ESA v5 processing in which an outlier filtering of Tb^{meas} was performed and it was able to mitigate part of the RFI biases. In the CATDS RE05 processing, a 3 σ_{Tbn} filtering is applied to (Tb^{meas}-Tb^{mod}) before performing the SSS retrieval. Some tests (not shown) performed on SSS retrieved from filtered and from non-filtered Tb datasets confirm that the correction presented in this paper is more efficient when used in conjunction with a Tb filtering.

3.2 K2016 land-sea contamination correction

In this section, we briefly review the K2016 methodology. The K2016 correction aims at mitigating systematic errors constant with time and was shown to efficiently correct land-sea contamination in many regions. Given the 18-day sub-cycle of SMOS, a given location over the ocean is observed with the same SMOS measurement geometry every ~18 days; within

18 days, it is sampled by several SMOS SSS measurements which are located at various locations across the swath, x_{swath}. The K2016 methodology considers that the long term (2010-2014) SSS variability observed by SMOS has to be rather similar whatever x_{swath} and the orbit orientation x_{orb}. Relative biases, b_{land}, with respect to a reference SSS, $SSS_{ref,}$ are derived from SMOS SSS through a least square minimization approach, and through a series of iterations that will be described below. A consistent set of SMOS SSS, SSS_{K2016}, is obtained as:

$$SSS_{K2016}(t, \phi, \lambda, x_{swath}, x_{orb}) = SSS_{ref}(t, \phi, \lambda) - b_{land}(\phi, \lambda, x_{swath}, x_{orb}) \quad (2)$$

where t is the time of the measurement, ϕ, and, λ, are respectively the latitude and the longitude of the considered location over the ocean. x_{swath} is sampled within 25 km wide bins.

b_{land} and SSS_{ref} are derived as follows. Defining $p=(SSS_{ref}, b_{land})^T$, p_0 the *a priori* values of p, y_0 the SMOS SSS, the estimated values of p , p_{est}, are derived as:

$$p_{est} = p_0 + C_p . G^T.(G.C_p.G^T + R)^{-1} .[y_0 - f(p_0)] \quad (3)$$

where G is the matrix of derivatives of observations with respect to the parameters (also called observational operator), R is the covariance matrix for the observation error, C_p is the covariance matrix for the a priori error on the parameters p. C_p is parametrized as a function of an acceptable standard deviation of SSS, σ_{SSSref}, over a correlation timescale τ.

The minimization is repeated four times, twice with τ=16 days (corresponding to a 18-day Gaussian smoothing window), then twice with τ=8 days (corresponding to a 9-day Gaussian smoothing window). At each iteration, a new set of *a priori* values for p and for σ_{SSSref} are computed. During the first iteration, the *a priori* values of SSS_{ref}, SSS_{ref0}, are taken as the median of SMOS SSS at the center of its swath over the 2010-2014 period, the *a priori* value

of b_{land} is equal to 0, σ_{SSSref} is taken equal to 0.3 pss, and the observation errors are taken equal to the theoretical error associated with the L2 SMOS SSS retrieval, E_{SSS_L2}. SSS_{ref1} and b_{land1} are computed from the p and σ_{SSSref} solutions of the first iteration. During the second iteration, SSS outliers, linked primarily to RFI contamination, are detected using a 3-sigma outlier detection: if the difference between the L2 SMOS SSS and (SSS_{ref1}-b_{land1}) is larger than 3 times E_{SSS_L2}, the error on the measurement indicated in the matrix R is artificially increased. SSS_{ref2} and b_{land2}, estimated at the end of step 2, are used to produce the 18 day SSS_{K2016} fields. The third and fourth iterations aims at optimizing SSS_{ref} and b_{land} at 9 day resolution. During the third iteration, SSS_{ref2} and b_{land2} are taken as *a priori* parameters, τ is reduced to 8 days and σ_{SSSref} is increased to 0.5 pss resulting in SSS_{ref3} and b_{land3}. The fourth step leading to SSS_{ref4} and b_{land4} is similar to the second one using the same a priori values as in step 3. At the end, an additional term is added to the estimated bias, to ensure that the 4-year (2010-2014) median average of SSS_{K2016} equals the 4-year median average of ISAS SSS for each latitude and longitude:

$$b_{land}(\phi, \lambda, x_{swath}, x_{orb}) = b_{landx}(\phi, \lambda, x_{swath}, x_{orb}) - (\mathrm{med}(SSS_{ref}(t, \phi, \lambda)) - \mathrm{med}(SSS_{ISAS}(t, \phi, \lambda))) \quad (4)$$

with b_{landx} equals to b_{land2} in the case of 18-day corrected field estimates, or to b_{land4} in the case of 9-day corrected fields. Note that the last term of Equation (4) is the only external information used in the entire correction process and does not modify the temporal variability of the observed fields.

The K2016 methodology was developed based on SMOS SSS processed with ESA L2OS version 550. In order to provide consistent comparison of the K2016 corrected SSS (SSS_{K2016}) and the newly corrected dataset presented in this paper (SSS_{J2018}), SSS_{K2016} was re-computed using the L2 SMOS SSS version used for SSS_{J2018} i.e. CATDS RE05.

3.3 New correction

In the present paper, we add a correction for seasonally-varying latitudinal biases, b_{lat}, and we update the land-sea contamination correction, b_{land}, with respect to K2016. b_{lat} and b_{land} are assumed to be additive, so that the corrected SSS, SSS_{J2018}, is expressed as:

$$SSS_{J2018}(t, \phi, \lambda, x_{swath}, x_{orb}) = SSS_{ref}(t, \phi, \lambda) - b_{land}(\phi, \lambda, x_{swath}, x_{orb}) - b_{lat}(\phi, x_{swath}, x_{orb}, m) \quad (5)$$

where m is the month of the SMOS pass. In a last step, similar to K2016 (equation 4), the 7-year (2010-2016) median average of the corrected SSS is adjusted, for each latitude and longitude, to the 7-year median average of ISAS SSS. The latter is the only quantitative information external to SMOS data used in the correction process and does not modify the temporal variability to the observed fields.

3.3.1 Observed seasonally-varying latitudinal biases

Further than 1000 km from the coastline, land-sea contamination is not detectable but seasonally-varying latitudinal biases are observed. They mostly depend on x_{swath}, x_{orb}, and the month of the year. The two examples on Figure 2 illustrate the behavior for two extreme cases. In November (Figure 2 a-c), in the center of the swath, SMOS SSS latitudinal variations are very close to ISAS SSS latitudinal variations on ascending orbits but not on descending orbits. In January (Figure 2 b-d), descending orbits at the edge of the swath display strong biases with respect to ISAS while ascending orbits do not. The systematic errors are quite stable from year to year, as indicated by the standard deviation of the 2011 to 2016 monthly latitudinal SMOS minus ISAS SSS difference (Figure 2c and d). It is not true at high latitudes where, in most cases, both the mean and standard deviation of the differences are high. This is likely associated with an effect of ice contamination. Systematic errors observed over other ocean basins are similar (see Appendix A1). These systematic

errors could originate from imperfect estimates of the sun or galactic noise contributions (Yin et al. 2013).

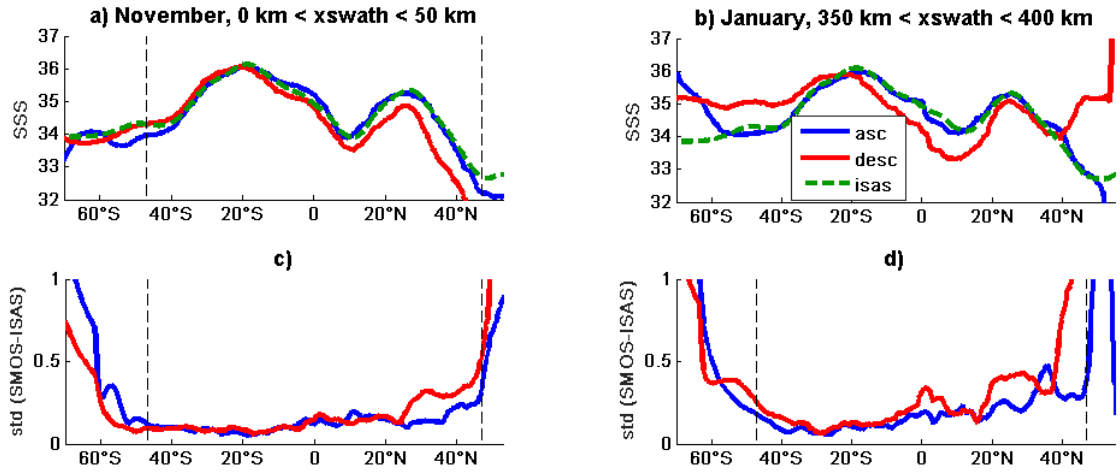

Figure 2 : Two examples of 2011-2016 latitudinal profiles of mean SSS (a; b) and of the standard deviation of the 2011-2016 monthly differences between SMOS SSS and ISAS SSS (c; d). The latitudinal means and standard deviations are computed over the Pacific Ocean further than 1200 km from any coast: green: ISAS, blue: SMOS ascending orbits; red: SMOS descending orbits: a;c) November; middle of the swath (0-50 km from the center of the swath); b; d) January; edge of the swath (350-400 km from the center of the swath). Dashed vertical lines indicate 47°N and 47°S.

3.3.2 Correction for seasonally-varying latitudinal biases

b_{lat} is determined separately for ascending and descending orbits, on a monthly basis, and is assumed to be independent of the longitude and of the year. We neglect interannual variations that could result from variation in sun activity, as they appear to be an order of magnitude smaller than the seasonal biases (see section 3.3.1). The correction is estimated from Pacific Ocean orbits further than 1200 km from continental coasts, in order to avoid land-sea contamination (b_{land} in Eqn 4 vanishes in this case) and because the northern latitudes in the Pacific Ocean are less affected by RFI than in the Atlantic Ocean. For x_{swath} locations and seasons not very affected by RFI at high latitudes, we checked that biases are similar in the

Pacific and Atlantic Ocean (see Appendix A1). For each x_{swath} and x_{orb}, twelve sets of monthly latitudinal corrections are estimated by comparing SMOS SSS on contaminated and non-contaminated x_{swath} intervals. The first step is to choose a set of non-contaminated x_{swath} for each month and for each x_{orb} that is used as reference in our correction methodology. The non-contaminated x_{swath} locations are identified from comparisons between 6-year averaged (2011-2016) monthly latitudinal SSS profile at 0.25° resolution derived for each SMOS x_{swath} location and from ISAS as described in Appendix A1. The 2010 year is not considered for the correction estimate as the calibration of the MIRAS instrument was not very stable during the SMOS commissioning period (January to June 2010). The latitudinal profiles of the unbiased SMOS SSS at reference x_{swath} locations determined for a given month, are averaged together to provide a reference SSS latitudinal profile. The latitudinal correction is then estimated as the median difference, per 5° latitude, over the EASE2 grid latitudinal sampling, between the latitudinal profiles of the SMOS SSS at contaminated x_{swath} and the reference SSS latitudinal profile. The SMOS SSS latitudinal profiles differ from the ones based on ISAS SSS at high latitudes (Figure 2). This difference may be explained by remaining RFI contamination in the northern latitudes but also by sea-ice contamination extending equatorward to about 1000 km from the ice edge. On ascending and on most descending latitudinal profiles, large differences between SMOS and ISAS SSS are indeed found poleward of 47°N (see two examples on Figure 2). Some degradation also occurs between 40° and 47ºN (see a worse case on Figure 2d). It concerns only a few x_{swath} and months on descending orbits and is therefore rather limited. In the Southern Ocean, in Spring and Summer (Figure 2a-b), large differences only appear way south of 47°S. However, in Winter, especially in the Atlantic Ocean where the ice edge can be as north as 55°S, large differences can reach 47°S. As a

compromise, in the following, the correction is applied only to latitudes within 47°S-47°N and results will be limited to this latitudinal range.

3.3.3 Updated land-sea contamination correction

Before estimating the land-sea contamination correction, we apply seasonally-varying latitudinal corrections determined as described in the previous section. Actually, an imperfect correction of sun and galactic noise effects is expected to generate systematic seasonal biases whatever the distance to the coast.

With respect to K2016, we make the following changes:

- In K2016, the covariance matrix of observation error, R, was filled with E_{SSS_L2} times the Identity matrix. With this approach, the observation errors depend only on the Jacobian of the modelled Tbs with respect to the retrieved parameters, on the a priori error on SMOS Tbs (equal to the SMOS radiometric noise) and on the a priori errors on auxiliary parameters. It does not take into account the actual differences between SMOS observed and modelled Tbs. In most cases, this difference is very close to the radiometric noise (e.g. Yin et al. 2012) and the associated χ (equation 1) normalized by the root mean square of N, χ_N, is close to 1. However, in case of polluted areas (e.g. RFI), χ_N becomes larger than 1. In the updated method, the errors specified in R are set to (E_{SSS_L2} .χ_N) in order to take observed mismatches between SMOS measured and modelled Tbs into account. In case χ_N is greater than 3, the particular SMOS SSS retrieval is not used in the correction estimate.

- In K2016, σ_{SSSref} was a fixed value (0.3 pss for τ=16 days; 0.5 pss for τ=8 days). σ_{SSSref} now uses an estimate of the SSS natural variability standard deviation, σ_{SSSnat}, as derived from SMOS measurements themselves. We derive σ_{SSSnat} using a two-step iterative procedure, in which we first compute debiased SSS using σ_{SSSref} =0.3 pss for each grid point over the whole period as before, then we recompute debiased SSS using σ_{SSSref} equal to the standard deviation of the debiased SSS from step 1. σ_{SSSnat} is taken as the standard deviation of the debiased SSS obtained in step 2. In the open ocean σ_{SSSnat} is very close to the value we used in the previous version (0.3 pss) (Figure 3 a), but it is much larger in regions characterized by large inputs of freshwater, such as river plumes (e.g. Amazon plume, Bay of Bengal, Gulf of Mexico), rainy areas (e.g. Intertropical Convergence Zone, eastern and western tropical Pacific fresh pools) and areas characterized by numerous mesoscale features (e.g. Gulf Stream, south east of the Arabian Sea). With this variable σ_{SSSref} we allow SSS_{ref} to vary more temporally in high variability regions through equation (3).
- The biases are derived from 7 years (2010-2016) of SMOS data instead of 4 years in K2016.

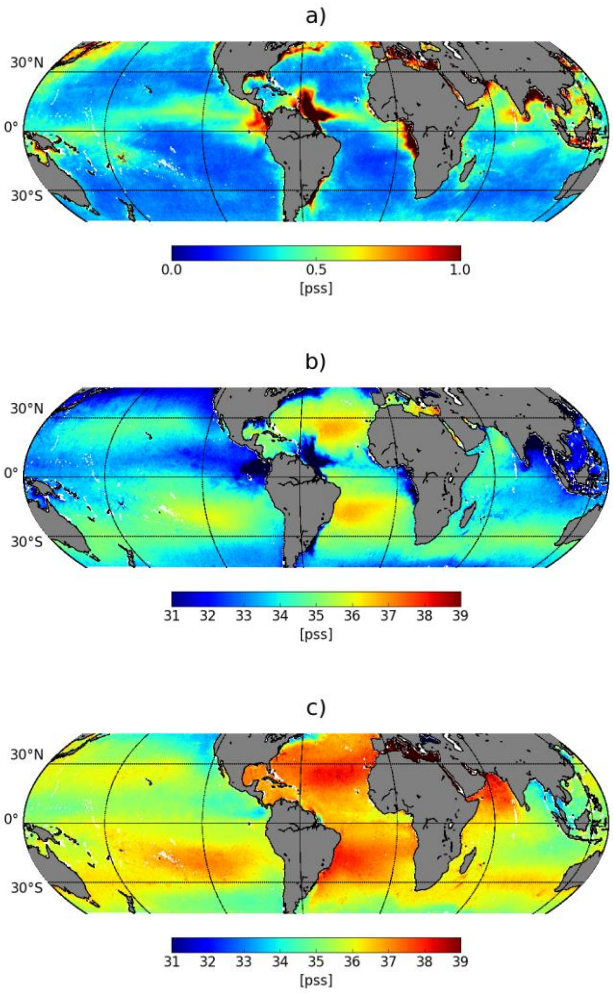

Figure 3 : a) SSS variability (σ_{SSSnat}) derived from 7 years of SMOS filtered and corrected SSS (after debiasing and filtering): large values are observed in river plumes and in rainy areas (ITCZ, SPCZ. b) Minimum and c) maximum of the SSS as derived from 18-day CEC LOCEAN that are used in the mapping of debiased near-real time products (see section 3.4).

3.4 Mapping methods

All SMOS level 3 maps shown in this paper include only SSS retrieved under moderate wind speed (3-12 m s^{-1}) and within +/-400 km from the center of the swath.

The non-bias corrected SMOS SSS is taken from the CATDS CPDC RE05 default processing. Daily SMOS SSS retrieved over ascending and descending orbits are combined to produce level 3 fields (L3P) (CATDS, 2017b). L3P fields over a 25x25 km^2 EASE 2 grid

424 are obtained from SMOS SSS weighted by E_{SSSL2} and averaged within monthly and ~ 10
425 days 25x25 km^2 bins. Measurements are filtered based on SSS retrieval quality flags and
426 avoiding regions suffering from major contaminations on Tb (e.g. galactic noise). A full
427 description of the procedure is available in Vergely and Boutin (2017).

428 Two sets of level 3 bias-corrected SMOS SSS fields are considered in this paper. The same
429 biases are applied (equation 5) but the filtering and mapping methods are different, partly due
430 to operational constraints in CATDS CPDC processing. One set, named L3Q, is processed in
431 near real time by the CATDS CPDC operational chain using a mapping procedure similar to
432 the one applied to L3P products. The other set, named CEC, is processed in delayed time by
433 the LOCEAN expertise center (CEC) of CATDS with a filtering and mapping procedure
434 similar to K2016. Hence, in the result section, changes brought by our new correction with
435 respect to non-corrected SSS will be evaluated by studying L3P and L3Q fields. Changes
436 with respect to K2016 methodology will be evaluated by studying K2016 and CEC fields.
437 The main characteristics of the L3P, K2016, CEC and L3Q processing are summarized in
438 Table 1.

439 Table 1: Summary of the main characteristics of the CATDS products and methods

	Original K2016	L3P	K2016 in this paper	CEC	L3Q
References					
CATDS Name	CEC LOCEAN debias_v0	CPDC L3P	-	CEC LOCEAN debias_v2	CPDC L3Q
Dataset reference	-	CATDS, 2017b	-	Boutin et al. 2017	CATDS, 2017c
Input data processing					
Level 1 data	ESA v5	ESA v6	ESA v6	ESA v6	ESA v6
Level 2 data	ESA v550	CATDS RE05 L2P	CATDS RE05 L2P	CATDS RE05 L2P	CATDS RE05 L2P
Tb outlier sorting	Yes	Yes	Yes	Yes	Yes
Correction Methodology					
Land-sea contamination correction	Yes	No	Yes	Yes	Yes
Latitudinal bias correction	No	No	No	Yes	Yes
Reference period	2010-2014	-	2010-2014	2010-2016	2010-2016
$\sigma_{SSSref0}$ (18-day)	0.3 pss	-	0.3 pss	σ_{SSSnat}	σ_{SSSnat}
Errors in R matrix	E_{SSS_L2}	-	E_{SSS_L2}	$E_{SSS\_L2} . \chi_N$	$E_{SSS\_L2} . \chi_N$
L3 fields					
Gridding method	Smoothing over R=50 km	Bin average (25 km grid)	Median nearest neighbors (25 km grid)	Median nearest neighbors (25 km grid)	Bin average (25 km grid)
Filtering	$SSS_{ref} \pm 3.E_{SSS\_L2}$	L2 flags	$SSS_{ref} \pm 3.E_{SSS\_L2}$	$SSS_{ref} \pm 3.E_{SSS\_L2}.\chi_N$	$SSSmax+2.(E_{SSS\_L2} . \chi_N)$ & $SSSmin-2.(E_{SSS\_L2} . \chi_N)$

440 *NB : The K2016 processing shown in the present paper has been recomputed from CATDS RE05 processing and using the same filtering as in
441 CEC product

We now describe in detail the mapping and filtering procedures for generating L3P and CEC fields:

- At the CATDS CEC LOCEAN, SSS gridded fields at 25x25 km^2 resolution, named CEC SSS in the rest of the paper, are built from the combination of debiased SSS which have been filtered from outliers in the course of the biases estimates (see description of steps 2 and 4 in K2016 methodology (section 3.2)). Debiased SSS are temporally averaged using a convolution with a Gaussian kernel with a full width of either 9 or 18 days at half maximum. In addition, a median filtering over nearest neighbors is applied to reduce remaining noise. CEC fields are built every 4 days over the 2010-2016 period (Boutin et al. 2017). From the 18-day CEC SSS fields over the 2010-2016 period, a minimum (SSSmin) and maximum (SSSmax) SSS is estimated at each grid point (Figure 3b and c) and is used to filter the operational CATDS CPDC products (see below).
- The CATDS CPDC operational chain provides near-real time data, at the expense of a less-refined data filtering. Biases are estimated as described previously and are applied (equation 4) to daily L3P SSS. For each orbit orientation, we define upper and lower acceptable bounds for daily SSS, based on acceptable absolute values and on SSS natural variability. The upper bound is the minimum value between 40 pss and SSSmax+2.(E_{SSS_L2} .χ_N); the lower bound is the maximum value between 5 pss and SSSmin-2.(E_{SSS_L2} .χ_N). SSS with (E_{SSS_L2} .χ_N) larger than 3 pss are filtered out. Level 3 SSS fields, named L3Q in the rest of the paper, are then obtained using a simple average of the SSS weighted by (E_{SSS_L2} .χ_N) over one month or ~ 10-day. A full description

of the procedure is available in Vergely and Boutin (2017). Corrected fields are produced in near-real time at various spatial resolution (CATDS, 2017c). In this paper we use the 25 km resolution products.

4. Comparison to ISAS

Before assessing the new CEC and L3Q SSS fields with products which are not used in the correction method, we compare the corrected and non-corrected SMOS SSS fields with ISAS SSS fields. The comparison is restricted to L3P and L3Q SMOS SSS fields because these two fields are mapped using the same methodology.

Even if ISAS SSS is used as a guide to choose the reference x_{swath} in the latitudinal correction, we recall that the only quantitative ISAS information entering our method is the 7-year median average of the ISAS SSS fields. The amplitude of temporal variability is independent of ISAS SSS variability. It is thus informative to compare the SSS temporal variability detected by SMOS and ISAS.

By construction, the 7-year mean SMOS minus ISAS SSS difference is expected to be small. It is nevertheless non-zero everywhere as we apply a more stringent filtering in the course of the correction estimate than in the L3Q bin average computation. At less than 800 km from coasts, the mean difference between SMOS SSS and ISAS SSS is reduced from -0.5 pss to -0.07 pss (Table 2). The remaining -0.07 pss difference is likely due to the lack of *in situ* measurement in very fresh areas in the vicinity of land (less than 2000m depth) and to non-Gaussian short-scale SSS variability smoothed out by ISAS objective mapping. In addition, SMOS samples the very near surface measurement (~ 1cm) while most *in situ* measurements used in ISAS analysis are performed close to 5m depth (Boutin et al. 2016). The standard

deviation of the differences (Figure 4 a & b) is much reduced in the vicinity of continents, except in river plumes areas but there, it could be an effect of ISAS smoothing.

Table 2: Statistics of monthly SMOS SSS (only pixels with more than 8 SMOS SSS retrievals in ascending and descending orbits are considered) minus ISAS SSS ; 2010-2016

	Number of pixels	Mean bias (SMOS – ISAS)	std(SMOS-ISAS)
45°S-45°N distance to coast <800 km			
SMOS without correction (L3P)	1542456	-0.53	0.63
SMOS with correction (L3Q)	1917346	-0.07	0.49
45°S-45°N distance to coast >800 km			
SMOS without correction (L3P)	5316809	-0.10	0.26
SMOS with correction (L3Q)	5429659	-0.02	0.20

In order to more precisely quantify the improvements between the L3Q and L3P SMOS SSS, we detect the number of months, N, between July 2010 and December2016, for which the absolute value of the difference between the L3Q and the L3P SSS is larger than a threshold, T equal to 0.2 pss (Figure 4).

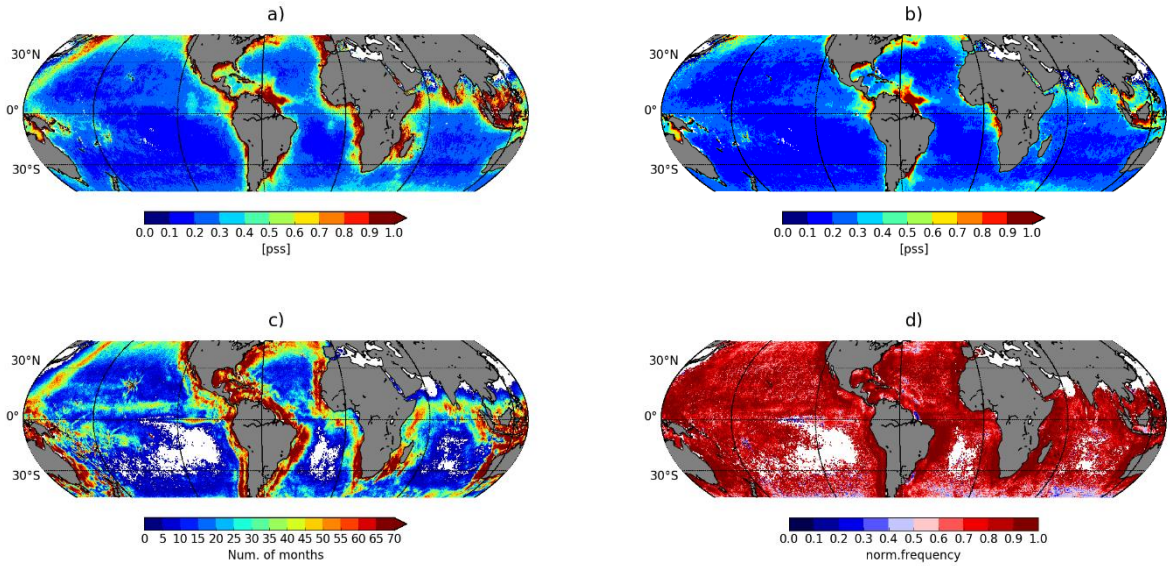

Figure 4 : Monthly SMOS SSS compared to monthly ISAS SSS from July 2010 to December 2016. Standard deviation of the differences for a) L3P SMOS SSS; b) L3Q SMOS SSS. c) Number of months with differences between L3P and L3Q SMOS SSS greater than 0.2 pss. d) Frequency with which corrections identified on Figure c) correspond to decreased bias with respect to ISAS (i.e. L3Q SMOS SSS closer to ISAS SSS than L3P SMOS SSS): red color means that the correction improves most of the time; blue color means that the correction degrades most of the time. Blank colors in figures c) and d) mean no change above the 0.2 pss threshold or no data in the L3P version (the comparison is done only for valid L3P SSS).

As expected, the number of months affected by the correction in a given pixel is higher in the vicinity of continents. In a next step we evaluate how frequently the changes correspond to improvements. For these months significantly affected by the correction, we thus compute the number of months with L3Q SSS closer to SSSisas than to L3P SSS. In most areas, the correction brings monthly SMOS SSS closer to monthly ISAS SSS in 60% to 100% of the cases (Figure 4d). This is not true in the Gulf Stream region close to 40°N, probably because ISAS is not able to reproduce SSS mesoscale variability recorded by SMOS (Reul et al. 2014b), nor close to 10°S in the western Pacific Ocean and in the middle Indian Ocean, two regions strongly affected by RFI. It is nevertheless remarkable that other regions affected by RFI such as the north-western Pacific Ocean are improved most of the time, suggesting that the RFI disturbances there are sufficiently stable in time to be partly mitigated by our correction.

5. Assessment of the corrected fields

5.1 Comparison to SMAP SSS

SMAP CAP SSS has a similar spatial resolution as SMOS CEC SSS, SMAP passes are at 6AM and 6PM local time like SMOS, so that the spatio-temporal sampling of SMOS and SMAP are really comparable. SMAP SSS are much better filtered from RFI, hence providing an unprecedented monitoring of main river plumes in the vicinity of continents. On the other

524 hand, SMAP Tb calibration is more challenging than for AQUARIUS (Fore et al. 2016a), so
525 that the absolute value of SMAP SSS may remain imprecise to about 0.2 pss in low to mid-
526 latitudes of the open ocean, but biases up to 0.45 pss, which origin remains unclear, have also
527 been reported during certain periods in the Bay of Bengal (Tang et al. 2017, their Figures 5
528 and 12 respectively). It is out of the scope of this paper to study SMAP CAP SSS biases. We
529 focus the investigation on the SSS variability measured by both sensors.

530 The various SMOS SSS fields are compared with SMAP SSS fields over the period between
531 April 2015 and December 2016. Two ranges of temporal resolutions are considered, one
532 close to one week, another one close to 18 days. The choices of the average durations are
533 guided by the satellite repetitive orbit cycle and sub-cycle in order to get, for each instrument,
534 the most even spatial coverage. In the following, for simplicity, 10-day L3P, L3Q and 9-day
535 CEC SMOS SSS fields compared with 8-day SMAP SSS fields are referred to as 'weekly'
536 comparisons. Comparisons between 18-day SMOS SSS fields from K2016 and CEC
537 processing with 16-day SMAP SSS are referred to as 'bi-weekly' comparisons. We always
538 compare fields centered on the same time (at ±12 hours), in order to minimize the effect of
539 the different durations.

540 At global scale and 'weekly' resolution (Figure 5), standard deviations of the SMOS minus
541 SMAP SSS differences are reduced in the vicinity of large continents and of RFI sources (e.g.
542 Fiji island, Hawaï island, south of Madagascar) from more than 0.6 pss before correction
543 (L3P, Figure 5 b) to less than 0.4 pss after correction (L3Q, Figure 5 e; CEC, Figure 5 h)
544 becoming comparable to open ocean values. In addition, the number of valid pixels is
545 increased, especially in the vicinity of large continents (Figure 5 c, f and i). The improvement
546 is better with CEC fields than with L3Q fields due to the improved filtering. The square of
547 the Pearson correlation coefficient, r^2, is as good or better when considering L3Q instead of

548 L3P SSS (Figure 5 d and a). r^2 indicates the proportion of variance contained in SMAP SSS
549 that is explained by SMOS SSS. Hence, if the natural SSS variability is low relatively to the
550 satellite SSS noise, r^2 is expected to remain small whereas if the natural variability is large
551 compared to the satellite SSS noise, r^2 is expected to increase. This is what is observed. r^2 is
552 in particular increased from less than 0.5 to above 0.5 in the north of the Gulf of Mexico, in
553 the Gulf of Guinea, in the Bay of Bengal (no valid measurements exist there in the L3P
554 processing) and to the north of the Amazon plume. The improvement is even larger when
555 considering CEC SSS (Figure 5 i) instead of L3Q SSS due to the different filtering and
556 mapping procedures: then, r^2 in the above-identified regions becomes higher than 0.8. These
557 large values of r^2 correspond to regions of large natural SSS variability, much larger than the
558 SSS noise, as will be shown below. On the other hand, in most regions of the open ocean
559 where SSS variability is on the same order or smaller than SSS noise, r^2 remains small. If
560 instead of considering all the available SMOS SSS pixels (Figure 5), the comparison is made
561 using only SSS pixels available in every SSS products (Appendix A2), the standard
562 deviations of the differences are comparable or slightly lower in regions polluted by RFI but
563 this is at the expense of many measurements which contain meaningful variability as
564 indicated by high r^2 on Figure 5.
565 Figure 5 indicates a clear improvement of L3Q and CEC fields with respect to L3P fields. In
566 comparison with K2016 (not shown), standard deviations of the SMOS CEC 18-day SSS
567 minus SMAP SSS differences are very similar (within +/-0.05 pss) in major parts of the
568 ocean, but in the regions identified above where r^2 became larger than 0.8, they are locally
569 improved by more than 0.5 pss; these regions are further studied below. We observe some
570 degradation (standard deviations of the SMOS minus SMAP SSS differences increase by up
571 to 0.3 pss) in some regions (the Mediterranean Sea, the Arabian Sea, the north-western part of

572 the Pacific Ocean) strongly affected by RFI and for which L3P fields do not provide valid
573 measurements. In these regions, however, r^2 obtained with both CEC and K2016 versions
574 remain less than 0.2.

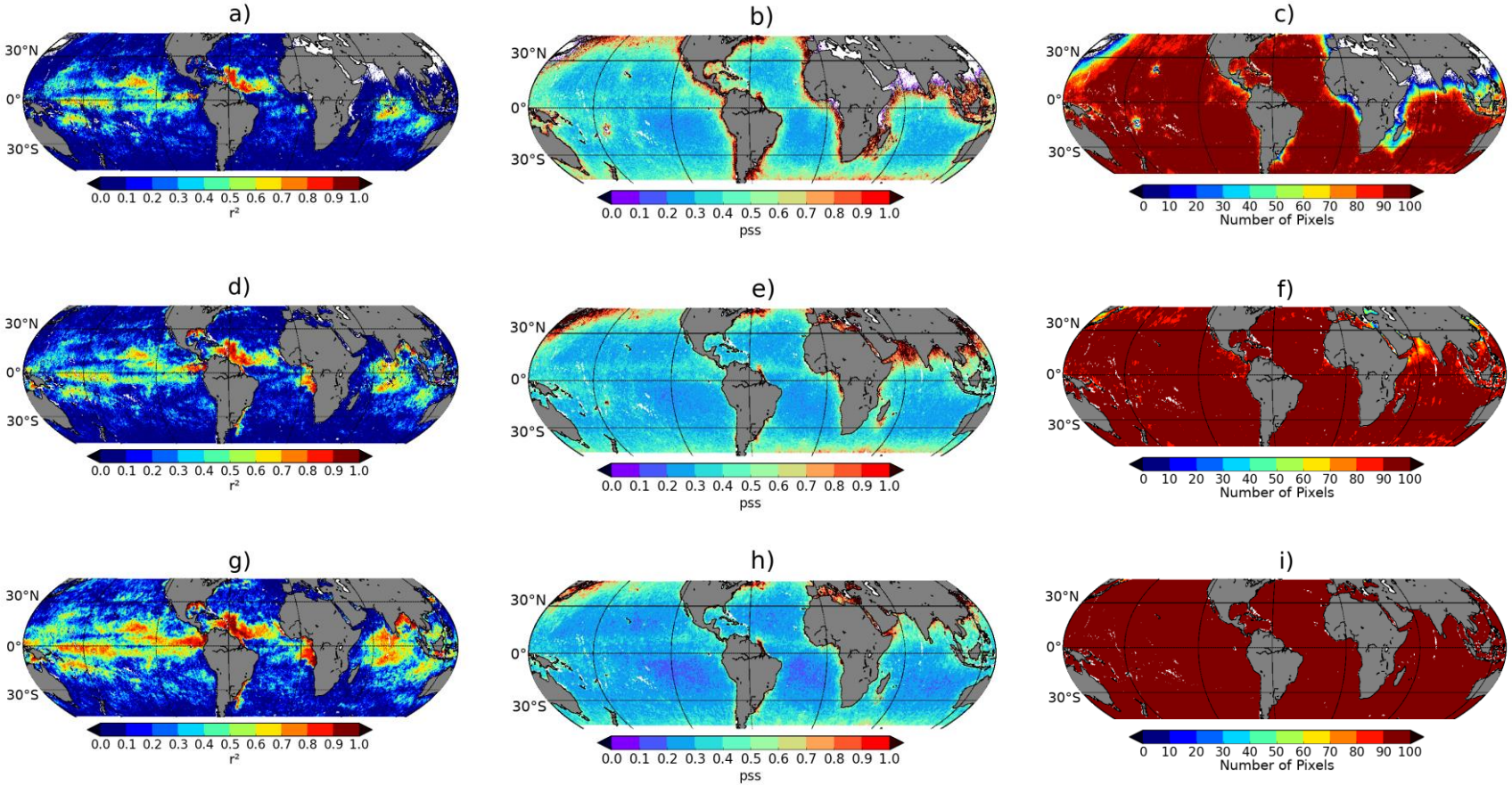

575 Figure 5: Comparison of SMOS and SMAP 'weekly' SSS: (a, d, g) r^2, (b, e, h) standard deviation of the differences, (c, f, i) number of pixels used in the
576 comparisons. (a, b, c) 10-day L3P SMOS SSS, (d, e, f) 10-day L3Q SMOS SSS, (g, h, i) 9-day CEC SMOS SSS. Same indicators but when considering only
577 the pixels available in the four products are presented in Appendix A2.

We now detail more quantitatively the comparisons between SMAP and SMOS K2016 / CEC SSS in four regions with very variable salinities (Bay of Bengal; Gulf of Mexico; Eastern Tropical Atlantic Freshwater Pools; Amazon plume), identified on Figure 5 as having a high r^2 after correction and already presented in the introduction. Contamination by RFI is very strong in the Bay of Bengal and in the Eastern Tropical Atlantic Freshwater Pools (see very small number of valid L3P measurements (Figure 5c)) and moderate in the two other regions. The coast geometry is very different in these 4 regions: the Bay of Bengal and Gulf of Mexico are semi-enclosed ocean areas so that land-sea contamination of an ocean pixel is expected to come from more than 290° of different directions, while the other two regions are surrounded in more than 180° around the points by the ocean.

As shown on the maps of Figure 1 and on the corresponding scatter plots (Figure 6, two left columns), the new SMOS CEC SSS captures fresh SSS patterns much closer to the ones in SMAP SSS and remains close to SMAP SSS in other SSS ranges. For instance, in the Bay of Bengal (Figure 1 a-c), the comma-shaped fresh SSS around 85°E and 17°N corresponds to fresh water originating from the Ganges-Brahmaputra trapped in an eddy (Fournier et al. 2017) and the one near 15°N, 95°E, to the Irrawady discharge. In the Gulf of Mexico (Figure 1 d-f), the horseshoe-shaped fresh SSS coming from Texas flooding and transported by ocean currents (Fournier et al. 2016) is better captured, as well as the Eastern Tropical Atlantic Freshwater Pools (Figure 1 g-i) and the Amazon and Orinoco plumes (Figure 1 j-l). The statistics of the SMOS SSS minus SMAP SSS differences are reported in Table 3. The median of the differences between SMOS and SMAP SSS and std(SMOS-SMAP) are decreased in all regions. The L1 norm estimator std1 (equal to median(abs(x-median (x)))/0.67, and that is less affected by the outliers than std), and r^2 are clearly improved in the Bay of Bengal; the improvement is less in other regions because of the larger proportion of

602 higher SSS values, and less stringent noise filtering at moderate SSS. For SSS less than 25pss
603 in the Amazon plume and in the Bay of Bengal, SMOS SSS remains in some cases higher
604 than SMAP SSS.

605

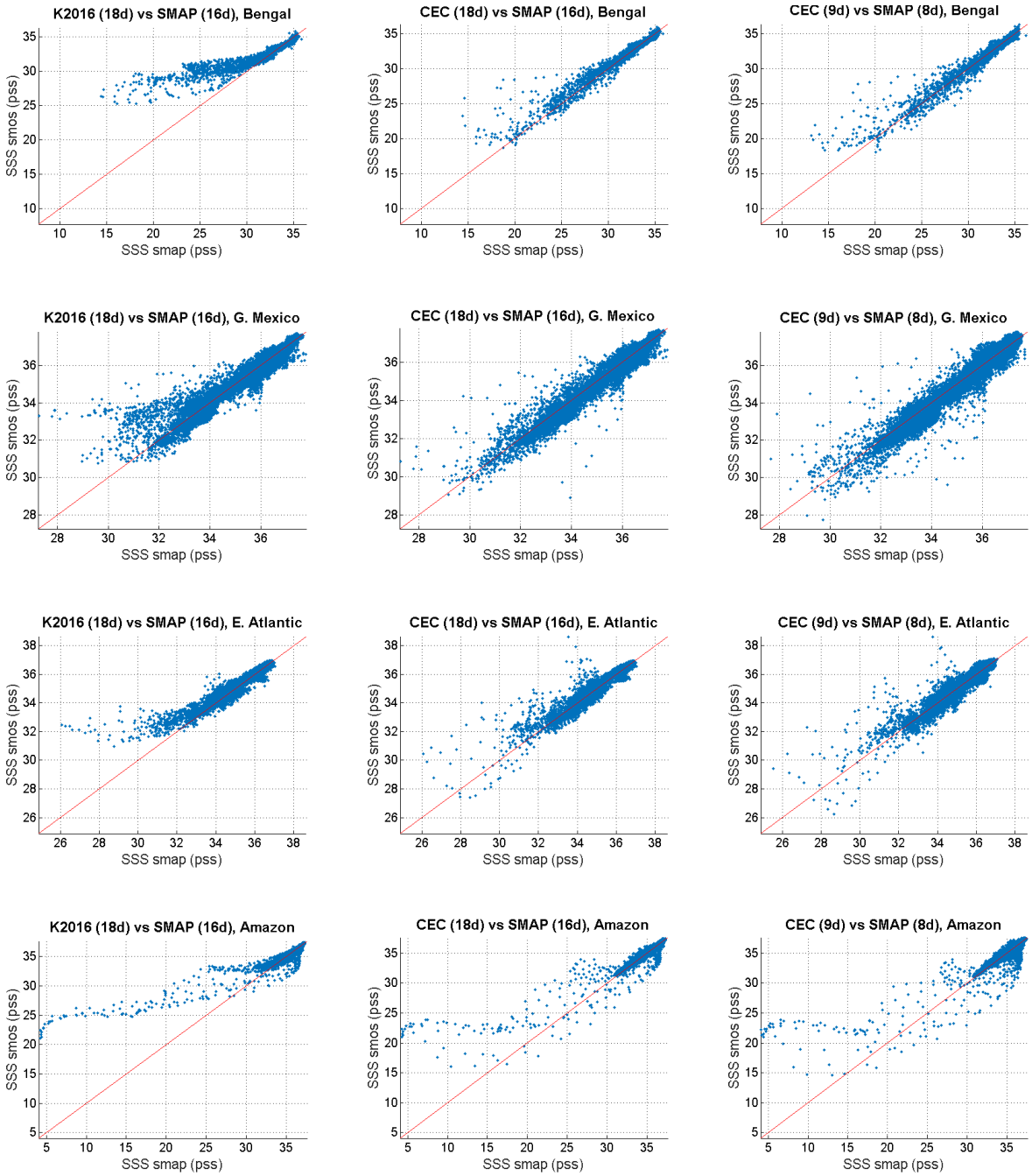

606 Figure 6 : Scatter plots of SMOS corrected fields versus SMAP SSS on the 4 regions and fresh events
607 periods illustrated on Figure 1: first line: Bay of Bengal; 2nd line: Gulf of Mexico; 3rd line : Eastern
608 Tropical Atlantic Freshwater Pools; 4th line : Amazon plume. First column: SMOS K2016 SSS;
609 second column: SMOS 18-day CEC SSS; last column: SMOS 9-day CEC SSS.

610 Table 3: Statistics of (SMOS SSS – SMAP SSS) corresponding to scatter plots of Figure 6

K2016 (18d) – SMAP (16d)				CEC (18d) - SMAP (16d)				CEC (9d) - SMAP (8d)			
median	std	std1	r^2	median	std	std1	r^2	median	std	std1	r^2
Bay of Bengal											
0.10	2.00	0.56	0.85	0.02	0.77	0.38	0.95	-0.03	0.81	0.41	0.95
Gulf of Mexico											
-0.02	0.50	0.29	0.90	-0.06	0.39	0.30	0.94	-0.06	0.45	0.37	0.93
Eastern Tropical Atlantic Freshwater Pools											
0.04	0.42	0.23	0.92	0.01	0.39	0.23	0.91	0.05	0.44	0.29	0.90
Amazon Plume											
-0.14	1.00	0.20	0.83	-0.13	0.82	0.20	0.85	-0.11	0.87	0.25	0.80

611

612 The time series of the indicators reported in Table 3 are plotted for each case study region on
613 Figure 7 to Figure 10. 'Bi-weekly' indicators confirm that during periods with large SSS
614 variability detected by SMAP (black line on top right figures) and low SSS (black line on top
615 left figures), r^2 (bottom left figures) and std(SMOS-SMAP) (bottom right figures) are
616 systematically improved for CEC with respect to K2016: r^2 becomes larger than 0.9 except in
617 the Amazon plume (~0.8). This is not systematically the case during periods with low SSS
618 variability and salty SSS when sometimes K2016 performs slightly better in term of r^2 and
619 std(SMOS-SMAP): this is likely because our method neglects seasonal variation of σ_{SSSnat}.
620 Nevertheless, the worse r^2 obtained with CEC SSS relative to K2016 SSS correspond in
621 reality to weak degradations of the corrected SSS, given the noise in both SMOS and SMAP
622 SSS and the low SSS variability; on the contrary, the improved r^2 correspond to very
623 significant improvements in the detection of fresh SSS in highly variable regions.

std1 (dashed lines on bottom right figures) is on the order of 0.3 pss, which is consistent with a noise on each 'bi-weekly' satellite SSS product on the order of 0.2 pss. Tang et al. 2017 found a standard deviation of 0.17 pss between monthly SMAP and moorings SSS over the open ocean, a value comparable to the one we find with monthly-100 km SMOS-ship comparisons that will be described in section 5.2.

The standard deviations of the SSS (SSS std (top right figures)) obtained with CEC products are much closer to the SSS std of the 'weekly' SMAP products than the ones obtained with the 'bi-weekly' K2016 products during highly variable periods; during periods with low variability all SSS std are very close to each other. Nevertheless, except in the Gulf of Mexico, SSS std are slightly larger for SMAP SSS than for CEC SSS. This possibly indicates that our method still underestimates SSS natural variability in some cases. This may also be due to the adjustment to the 7-year median of ISAS SSS: for instance, the fresh water along the Brazil coast at 50°W-5°N is observed as a continuous tongue in the SMAP SSS map (Figure 1l), and as a discontinuous one in the SMOS SSS maps (Figure 1j - 1k) which is due to a discontinuity in the 7-year median of ISAS SSS (not shown). Further validation with external ground truth of SMOS and SMAP SSS would be necessary to confirm the origin of this discrepancy.

It is also instructive to consider the statistics obtained with 'weekly' products (Figure 6, right column and Figure 7 to Figure 10, blue lines) as SSS during periods with large freshwater discharges can be very variable at short time scales. In most cases, r^2 and std(SMOS-SMAP) obtained with 'weekly' products are slightly worse than the ones obtained with 'bi-weekly' products, because the noise is higher in the 'weekly' products but it nevertheless remains small relative to the natural variability. It is only in Fall, in the Bay of Bengal, when the SSS std is larger than 2.5 pss, that the r^2 and std(SMOS-SMAP) with the 'weekly' CEC product

are comparable to the r^2 and std(SMOS-SMAP) with 'bi-weekly' CEC product, the noise becoming negligible relative to the SSS natural variability. Hence, in very variable regions, the 'weekly' CEC maps could improve the monitoring of fresh spatial structures varying within 18 days.

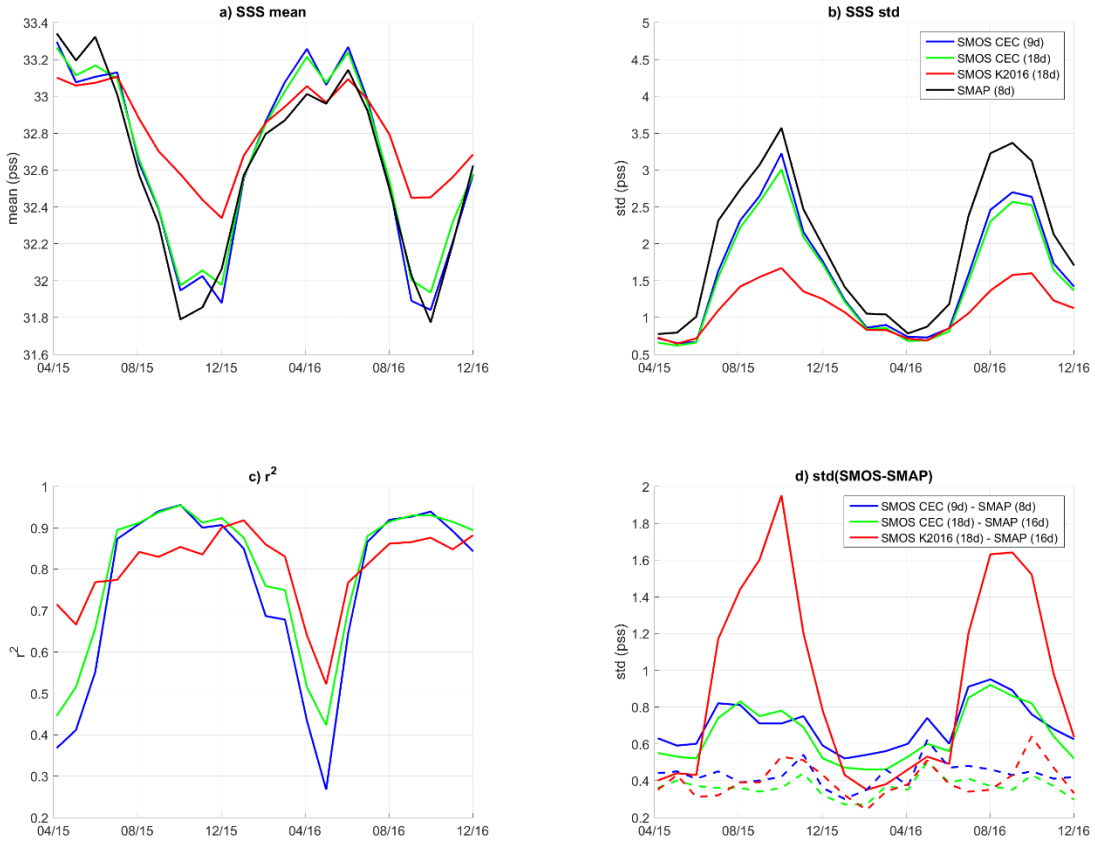

Figure 7: Time series of statistical parameters computed over the Bay of Bengal case study area, April 2015 to December 2016: a) mean SSS; b) SSS standard deviation; c) square of the Pearson correlation coefficient (r^2) between SMOS and SMAP SSS; d) Standard deviation of the SMOS minus SMAP SSS differences (plain line) using L1 norm (dotted line). 'Weekly' SMOS CEC(blue), 'bi-weekly' SMOS CEC (green), 'bi-weekly' SMOS K2016 (red), 'weekly' SMAP (black).

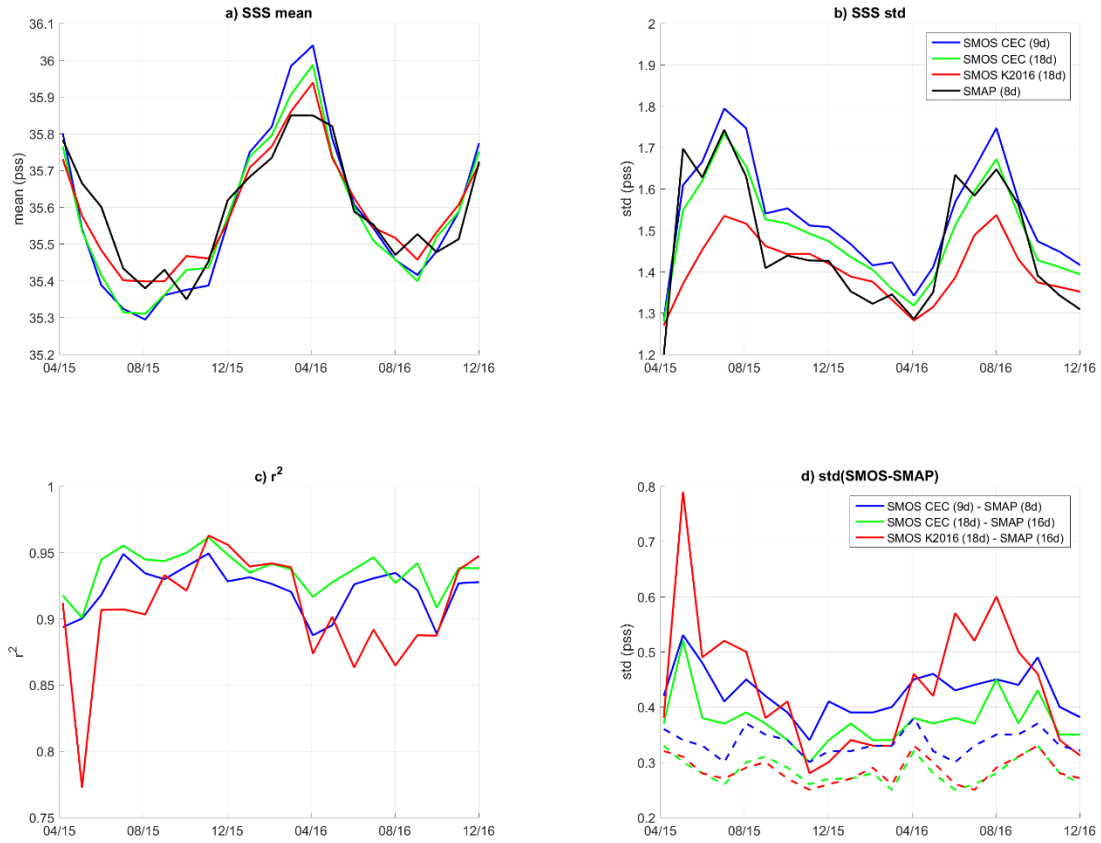

660

661 Figure 8: Time series of statistical parameters computed over the Gulf of Mexico case study area,
662 April 2015 to December 2016: a) mean SSS; b) SSS standard deviation; c) square of the Pearson
663 correlation coefficient (r^2) between SMOS and SMAP SSS; d) Standard deviation of the SMOS minus
664 SMAP SSS differences (plain line) using L1 norm (dotted line). 'Weekly' SMOS CEC(blue), 'bi-
665 weekly' SMOS CEC (green), 'bi-weekly' SMOS K2016 (red), 'weekly' SMAP (black).

666

667

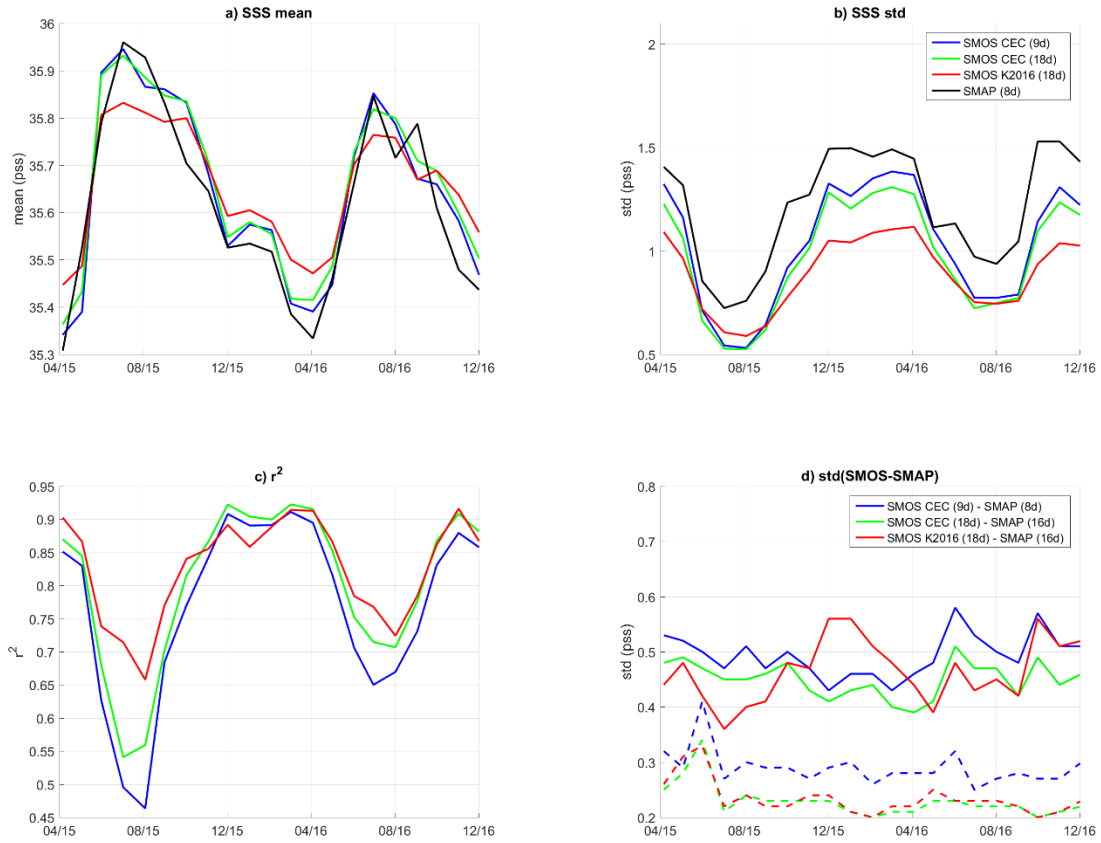

668 Figure 9: Time series of statistical parameters computed over the Eastern Tropical Atlantic Freshwater
669 Pools case study area, April 2015 to December 2016: a) mean SSS; b) SSS standard deviation; c)
670 square of the Pearson correlation coefficient (r^2) between SMOS and SMAP SSS; d) Standard
671 deviation of the SMOS minus SMAP SSS differences (plain line) using L1 norm (dotted line).
672 'Weekly' SMOS CEC(blue), 'bi-weekly' SMOS CEC (green), 'bi-weekly' SMOS K2016 (red),
673 'weekly' SMAP (black).

674

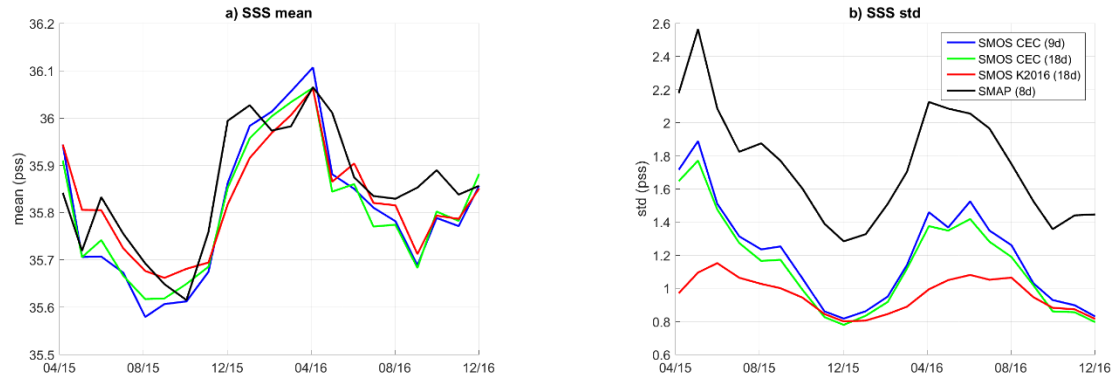

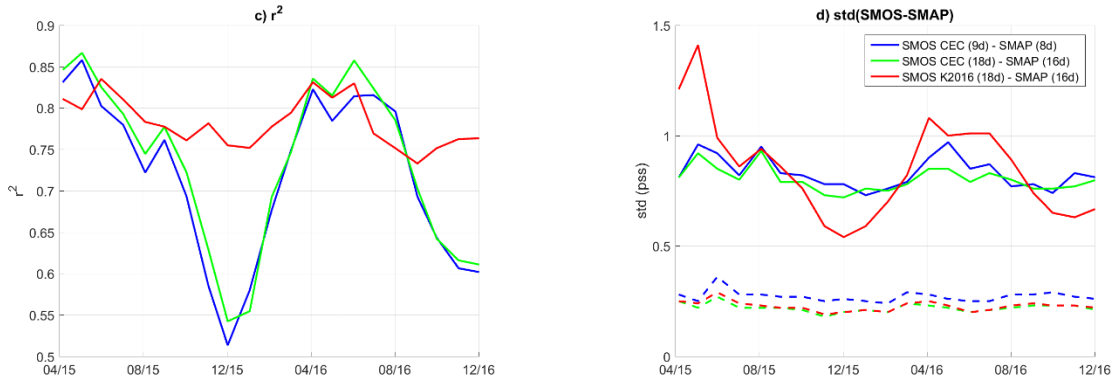

675 Figure 10: Time series of statistical parameters over the Amazon plume case study area, April 2015 to
676 December 2016: a) mean SSS; b) SSS standard deviation; c) square of the Pearson correlation
677 coefficient (r^2) between SMOS and SMAP SSS; d) Standard deviation of the SMOS minus SMAP
678 SSS differences (plain line) using L1 norm (dotted line). 'Weekly' SMOS CEC(blue), 'bi-weekly'
679 SMOS CEC (green), 'bi-weekly' SMOS K2016 (red), 'weekly' SMAP (black).

680

681 **5.2 Comparison to ship SSS**

682 Merchant ship transects are used to get ground-truth measurements at various distances from
683 the coast. With respect to SMAP SSS, ship SSS is less uncertain but its spatio-temporal
684 sampling and resolution is very different from SMOS SSS.

685 In a first step, we consider the scales of SSS variability captured by the various SMOS SSS
686 versions and by the ship SSS far from coast. We focus on the subtropical region (50°W-
687 20°W; 15°N-40°N) of the north Atlantic in 2013. This region is chosen because it is very
688 well covered by regular ship tracks spaced by approximately one month, it is strongly
689 impacted by the seasonally-varying latitudinal biases, it is characterized by mesoscale
690 variability that is not resolved by the ISAS analysis (Kolodziejczyk et al. 2015; Sommer et al.
691 2015), and it is not used for choosing the reference dwell lines of the seasonal latitudinal
692 correction. We analyze below the density spectra (Figure 11, top) and the squared coherence
693 (Figure 11, bottom) of ISAS, of 10-day L3P and L3Q, of 18-day CEC with ship SSS. Our
694 analysis focuses on wavelengths between 1400 km and 150 km, in order to minimize the

695 influence of the limited length of the selected ship tracks (about 2800 km) and of scales
696 resolved by SMOS (50 km). We recall here that coherence quantifies the correlation between
697 two quantities for a given wavenumber band. While at 1400 km wavelength ISAS and ship
698 SSS are very coherent, due to the subsampling of Argo measurements (1 profile per 10 days
699 per 3°x3°) and to the horizontal scales of the optimal interpolation (~300 km), the ISAS
700 spectrum (Figure 11, top, green line) dramatically drops as well as its squared coherence
701 (Figure 11, bottom) for shorter wavelengths.

702 Whatever the wavelength, the density spectra (Figure 11 top) of the 18-day CEC SSS is
703 closer to the one of the ship SSS than the 10-day L3P and L3Q. The density spectrum of the
704 9-day CEC SSS is very similar to the one of the 10-day L3Q for spatial wavelengths between
705 150 and 330 km. For longer wavelengths, the density spectrum of 9-day CEC SSS is
706 intermediate between the 18-day CEC and the 10-day L3Q, indicating that at large scale,
707 where the temporal variability between 9 days and 18 days is expected to be small, the
708 different filtering and gaussian mapping applied to CEC products is more effective at
709 reducing the SMOS SSS noise than the min/max filtering and bin average mapping applied to
710 L3Q products. Up to 150 km, the density spectra of the 18-day CEC and ship SSS are in
711 remarkable agreement. This is in fact quite surprising because the MIRAS and TSG
712 instrumental noises are not expected to lead to the same SSS errors and because the temporal
713 sampling of SMOS (about 8 passes over 18 days) and of ship (~one transect per month) are
714 very different. Given the expected noise in level 2 SMOS retrieved SSS (0.6 pss), the median
715 filtering over nearest neighbor pixels at 25 km distance in the SMOS CEC product, and the
716 SMOS temporal sampling, the noise on the 18-day CEC SSS is expected to be on the order of
717 0.15 pss. Noise on individual ship SSS is estimated to be less, on the order of 0.08 pss (Alory
718 et al. 2015) but the temporal sampling is worse. Hence, the similarity in the two density

719 spectra suggests that the SSS error due to instrumental noise that is larger in SMOS than in
720 ship SSS, is compensated, over 18 days, by the better temporal sampling in SMOS than in the
721 ship data.

722 The squared coherence (Figure 11 bottom) of the 18-day CEC SSS is almost at the same level
723 (above 0.7) as the squared coherence of ISAS SSS at a 1400 km wavelength, and is always at
724 a higher and significant level for wavelengths up to 300 km. The 18-day CEC squared
725 coherence decreases with decreasing spatial wavelengths. This can be due to instrumental
726 noise, to the different temporal sampling of SMOS and ship and to spatially moving
727 structures within 18 days. The 18-day CEC squared coherence becomes not significant at
728 95% for wavelengths smaller than 300 km. Considering that at least 3 samples are necessary
729 to resolve a 300 km wavelength signal, this result indicates that 18-day CEC and ship SSS
730 capture similar scales of variability up to about 100 km. This is rather consistent with the
731 spatial integration of SMOS measurement (50 km) in addition to the median filtering over
732 nearest neighbor pixels at 25 km applied on CEC products.

733 The level of coherence is much less both with the 10-day L3P and L3Q products, due to a
734 lower signal to noise ratio.

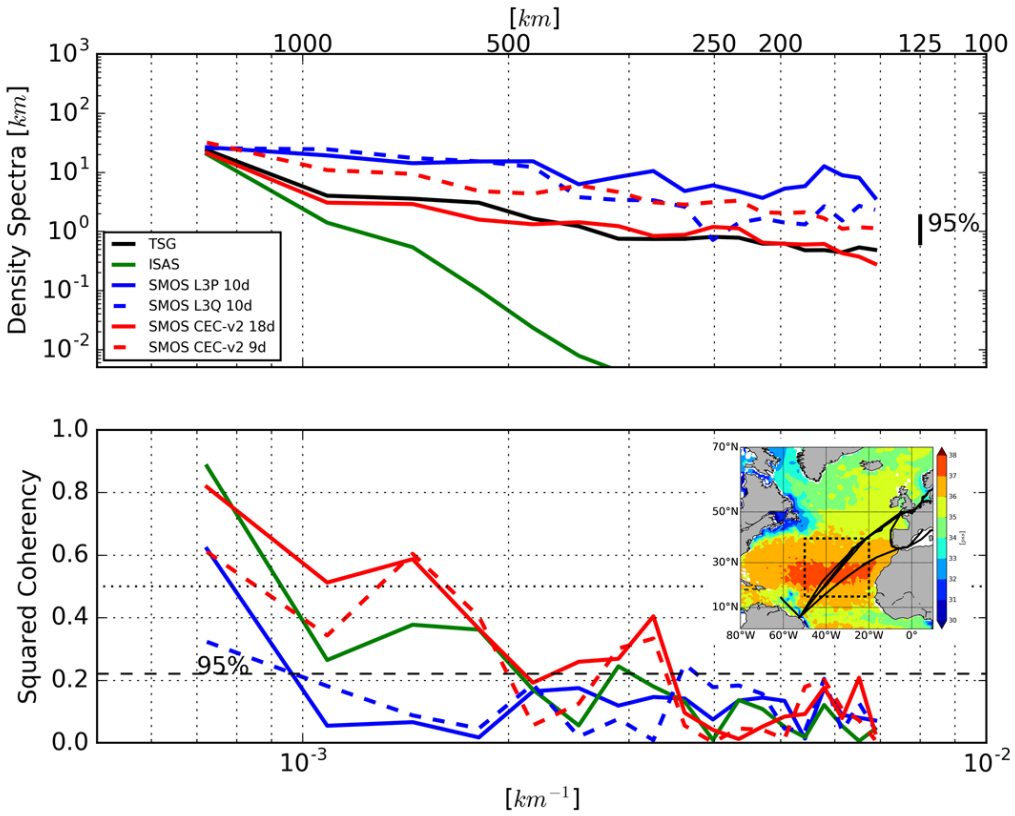

735

736 Figure 11 : Top: Density spectra; Bottom: Coherence between ship SSS and SMOS or ISAS SSS. The
737 spatial frequency (1/wavelength (km)) is indicated below the bottom plot, whereas the corresponding
738 wavelengths (km) are indicated above the top plot. Vertical dashed lines correspond to spatial
739 frequencies regularly spaced in logarithmic coordinates. Northern subtropical Atlantic (see box on the
740 color map) in 2013. Ship SSS measured on regular merchant ships transects (14 regular transects in
741 2013) (black), ISAS SSS (green), 10-day SMOS L3P (blue line), 10-day SMOS L3Q (dashed blue
742 line), 18-day SMOS CEC (red line), 9-day SMOS CEC (red dashed line).

743

744 We will now investigate global statistics for the difference between SMOS and ship SSS.

745 Consistent with the weak coherence observed between the ship SSS and the 10-day L3P and

746 L3Q SSS, 9-day CEC and 10-day L3P or L3Q are of worse quality than the 18-day CEC and

747 monthly L3P and L3Q fields. Hence, in the following comparisons, we only consider

748 monthly L3P, L3Q and 18-day CEC fields. Ships provide within a few hours numerous

749 measurements within a satellite pixel. In the following, the SSS variability sampled by each

750 ship and by SMOS is smoothed over +/-50 km. This smoothing cannot be identical for the

two platforms because of their different spatio-temporal sampling. SMOS observes a surface (two dimensions) whereas ship measurements are taken along a route (one dimension). However, this method is expected to reduce the misfit between in situ and SMOS observations coming from the spatial subsampling of SSS variability within a satellite pixel by point measurements (Boutin et al. 2016). Mean differences and standard deviation of the differences between SMOS SSS and ship SSS, named Std(SMOS-Ship) in the following, are shown in Figure 12, as a function of the distance from the coast. Two sets of comparisons are presented, involving either only SMOS pixels common to L3P fields (i.e. the ones the less affected by RFI pollution) (Figure 12, left) or all valid pixels for each product (Figure 12, right). The number of valid pixels is increased by nearly a factor 2 when approaching the coast with L3Q and CEC fields with respect to L3P fields (Figure 12, bottom right). The mean differences (Figure 12, top) obtained with monthly L3P are less than -0.5 pss up to 600 km from the coast. The mean differences with CEC fields are systematically less than 0.05 pss (in absolute value), further than 100 km from the coast, a very clear improvement with respect to L3P. Similar improvement is observed with monthly L3Q when considering only pixels common to L3P (Figure 12, left); the mean differences are, however, slightly more negative when considering all valid pixels, indicating that the filtering is more efficient at removing SSS outliers in CEC than in L3Q processing. At less than 100 km from the coast, the mean difference with CEC product reaches 0.15 pss, a value close to the mean difference between ISAS and ship SSS, consistent with local overestimate of the long term SSS mean by ISAS, as suggested by SMOS and SMAP SSS comparisons in the Amazon plume along the coast (Figure 1 and section 5.1). However, the scatter plot (not shown) between CEC and ship SSS in the region of the Amazon plume is very scattered at low SSS and it was not possible to identify a systematic bias.

775 Std(SMOS-Ship) is clearly improved whatever the distance to the coast. Further than 1000
776 km from the coast, it is equal to 0.20 pss with CEC, 0.21 pss with L3Q while it is 0.24 pss
777 with L3P. It increases when approaching the coast: in the 100-200 km class and when
778 considering all valid pixels, it equals to 0.64 pss with CEC, 0.69 pss with L3Q, 0.78 pss with
779 L3P. When approaching the coast, the ship SSS variability is increased too (black lines on
780 Figure 12, middle right) and it is likely that part of the Std(SMOS-Ship) induced by the
781 different temporal sampling of SMOS and ships increases when approaching the coast.
782 Consequently, while Std(SMOS-Ship) is increased by a factor 3 between 100-200 km and
783 further than 1000 km from the coast, the signal to noise ratio is increased by only a factor 1.5
784 between these two classes. Similarly, Std(SMOS-Ship) and ship SSS std are lower when
785 considering only L3P pixels than when considering all valid pixels, so that the signal to noise
786 ratio in both cases remains similar. When considering all valid pixels (Figure 12, middle
787 right), the std difference obtained with ISAS remains slightly less than the ones obtained with
788 CEC and L3Q SSS in all the classes considered except for the range from 500 to 900 km
789 (Figure 12, middle right). On the contrary, when considering only pixels common to L3P,
790 (Figure 12, middle left), CEC SSS better captures SSS variability than ISAS in all the classes
791 up to 900 km from a coast. Two typical ship comparisons illustrate these features. On Figure
792 13 (left), a transect in the South Pacific is quite well sampled by L3P, except between the
793 equator and 4°N where the L3Q and CEC SSS is closer to ship SSS. ISAS SSS appears to be
794 smoother than SMOS SSS, as expected from the optimal interpolation. On Figure 13 (right) a
795 ship transect crosses the North Atlantic Ocean in September 2013, a period of moderate RFI.
796 The L3P SSS is very discontinuous due to RFI disturbances in the north and to land-sea
797 contamination south of the equator. The L3Q and CEC SSS are more numerous and closer to

ship SSS than L3P SSS, even though the L3Q SSS appears to be more affected by RFI than the 18-day CEC SSS north of 40°N.

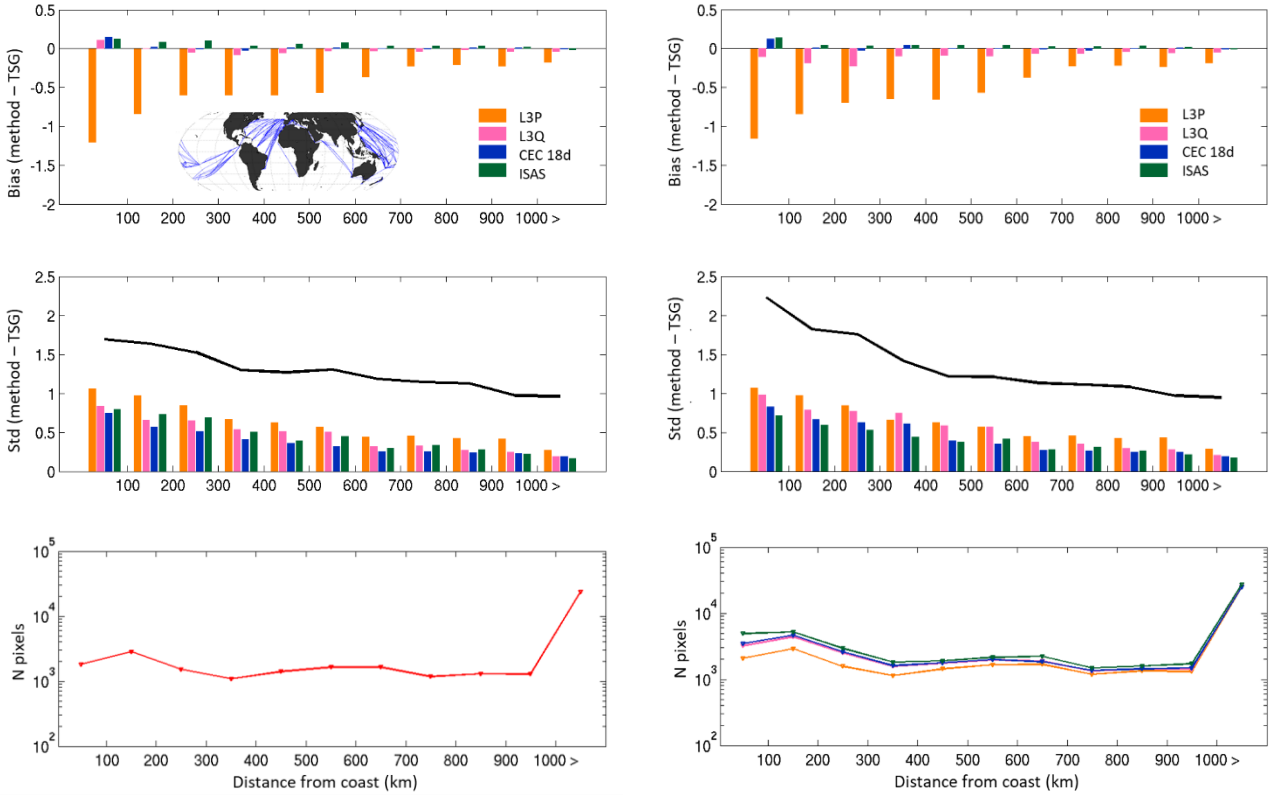

Figure 12 : Statistics of ship comparisons (May 2010-August 2016) binned as a function of the distance from the nearest coast: top) mean difference; middle) standard deviation of the differences; the black line indicates the standard deviation of ship SSS in each class; bottom) number of pixels used in the comparisons. Left: considering only the SMOS pixels common to all versions; right: considering all pixels available in each version. Ship and SMOS SSS are integrated over 100 km. Orange: monthly SMOS L3P ; pink : monthly SMOS L3Q; light blue : 18-day SMOS CEC; green : ISAS.

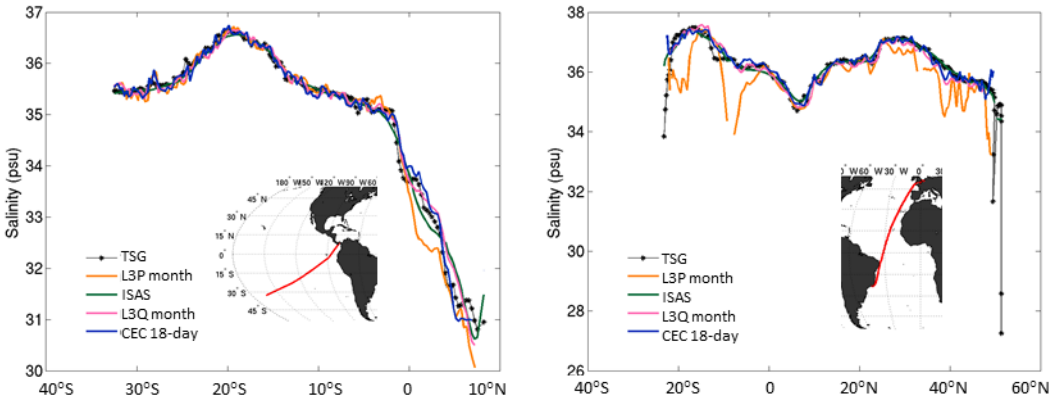

Figure 13 : Examples of comparisons between ship SSS (black stars line) and SMOS SSS: orange: non corrected (L3P), purple: monthly L3Q corrected, light blue :18-day CEC corrected; green : ISAS. Left) from 2014-08-21 to 2014-09-03, Matisse ship. Right) from 2013-08-21 to 2013-09-03, Santa Cruz ship. All SSS products have been smoothed over +/-50 km.

6. Discussion and Perspectives

Retrieving accurate SSS from SMOS measurements in the vicinity of continents is very challenging. The land-sea brightness temperature contrasts induce a contamination of the retrieved SSS signal, up to about 1000 km from the coast. This contamination is very variable across the SMOS swath. The origin of this pollution is very complex. It is likely related to an imprecise characterization of the 69 individual antenna patterns constituting the SMOS synthetic antenna, preventing a reliable theoretical modelling of the correction in the current SMOS image reconstruction process. The land-sea contamination has thus to be mitigated empirically. When doing so, the main difficulty is to distinguish the SMOS signal resulting from natural SSS variability from ones contaminated by RFI, whose sources are often located near coasts. To make matters worse, the typical RFI signature yields low SSS, and the largest SSS natural variability often occurs in low SSS regions, e.g. from river plumes or high rain regime. The K2016 methodology developed for correcting SSS affected by land-sea contamination was very efficient in many areas, but not in those characterized by strong

natural variability, as it implicitly assumed that natural SSS variability was negligible relative to SMOS SSS noise. The revised correction methodology presented in this paper includes information on the amplitude of natural SSS variability inferred from SMOS measurements. We further add a seasonally- and latitudinally-dependent bias correction.

The SMOS corrected SSS is much more consistent to the independent SMAP SSS than K2016, both in terms of SSS patterns and amplitude (Table 3). The SMOS SSS is, however, slightly noisier than SMAP: in the open ocean (Pacific ITCZ region), Supply et al. 2017 found an error of 0.6 pss on L2 SMOS SSS and of 0.5 pss on L2 SMAP SSS. This difference is explained by the radiometric accuracy of the respective instruments and by the SMAP flight hardware that allows efficient detection and filtering of most RFI (Mohammed et al. 2016) unlike SMOS. Nevertheless, both satellite missions record very similar SSS variability at weekly time scale that is not resolved by mapped Argo data (Figure 14). On average over 47°N-47°S, the standard deviation of the difference between SMOS CEC and ISAS SSS (Figure 14a) is 0.33 pss while the standard deviation of the difference between SMAP and ISAS SSS (Figure 14b) is 0.31 pss. The geographical distribution of this variability is very consistent with the small-scale variability of SSS observed by ship measurements (see Figure 6 of Boutin et al. 2016) with minima in the subtropics and maxima in coastal areas, in the vicinity of river plumes or in regions characterized by strong mesoscale fronts, such as the Gulf Stream.

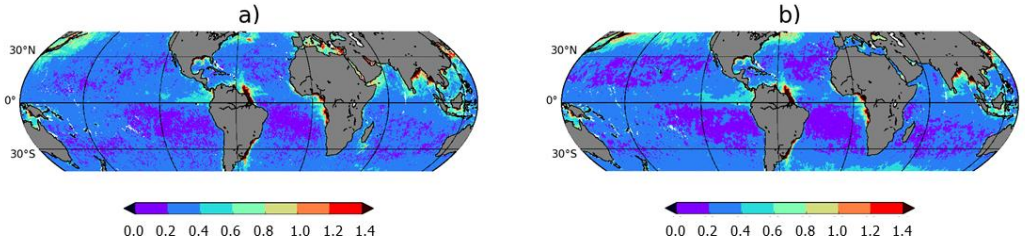

Figure 14 : Standard deviation of 'weekly' satellite SSS minus ISAS SSS between 47°N and 47°S, over the year 2016. a) SMOS CEC, b) SMAP CAP.

The only quantitative external information entered in the correction algorithm is the 7-year median of ISAS SSS that fixes the absolute calibration of the SMOS SSS in each pixel but does not influence its variability. In seasonally-varying latitudinal biases correction, ISAS SSS serves only in a qualitative way for choosing the SMOS cross-swath locations used as reference. The implemented correction removes most of the systematic errors and brings clear improvement when compared with *in situ* ground truths measurement or with SMAP SSS. Nevertheless, some refinements could still be envisioned. The absolute calibration based on ISAS median SSS leads to some inaccuracies in very near coastal pixels. This issue could probably be improved in the future by analyzing to what extent the absolute calibration is sensitive to the time period under consideration for computing the median and by merging information coming from ISAS SSS with other SSS fields. A further step could be taken by merging SMOS and SMAP information in order to build a level 4 product taking advantage of synoptic spatio-temporal coverage of satellite data for monitoring SSS variability and using *in situ* SSS for the absolute calibration of SSS fields. Future studies should also pay more attention to the bias seasonal and interannual variability as a function of sun activity and of land Tb variability which have been neglected in our study.

Our method corrects SMOS SSS retrieved with a Bayesian approach at level 2, as described in Zine et al. 2008 and as implemented in ESA and CATDS operational processors. Such a retrieval method takes advantage of the expected consistency between the various Tbs measured at various incidence angles at a given distance across the swath and takes the radiometric accuracy of each Tb into account. The land-sea contamination is expected to add variability and biases on the SMOS Tbs at a given distance across the swath, so that the

quality of the Bayesian retrieval is downgraded. In order to cope with this caveat, a systematic correction at Tb level has been implemented in ESA L2 OS processor v662, before the retrieval of SSS. The biases in the vicinity of land and the standard deviation of the difference with respect to ISAS are much reduced (Spurgeon and SMOS-Ocean Expert Support Laboratories, 2017), but flagged SSS (poor quality retrieval) remain in many coastal areas. Thus, the accuracy of the retrieved SSS is in general not as good as the one obtained with our correction at the SSS level (Level-3). The better performance of our methodology is likely due to the fact that we account for SSS variability. Given all the non-SSS geophysical effects affecting Tbs (roughness effect, galactic noise etc…), it is very difficult to account for SSS variability when dealing with Tbs measured at different angles within the field of view. Nevertheless, future work should explore a two-step correction, first performed at Tb level to improve the Bayesian L2 retrieval and second performed at SSS level.

An alternative debiasing method from a non-Bayesian approach has also been proposed by Olmedo et al (2017). Contrary to our approach, Olmedo et al. (2017) retrieve SSS from single angular Tb measurements, they filter SSS outliers using statistical indicators of the 3-year SSS histogram per incidence angle classes. They adjust the absolute value of SMOS SSS by adding the World Ocean Atlas climatology. An analysis (not shown) of the 9-day De-biased non-Bayesian SMOS SSS fields available from the Barcelona Expertise Center which have been obtained with an objective analysis in the regions and periods shown in Figure 1 indicates that the striking fresh features are captured at a similar level as what was obtained with K2016 methodology, consistent with the fact that the statistical indicators used to filter outliers do not depend on the SSS natural variability.

While SMAP SSS is expected to be much less affected by RFI, some disturbances remain in some regions (Mohammed et al. 2016) and the calibration of SMAP data is also challenging

(Fore et al. 2016b, Meissner and Wentz, 2016). Hence, when dealing with a local scientific study, dedicated comparisons with *in situ* ground truth are highly recommended in order to precisely estimate the validity of satellite SSS in a given region and period with respect to the natural variability that is considered. This should be facilitated in the future with the development of the SMOS PIlot Mission Exploitation Platform (PI-MEP).

The CATDS/CPDC L3Q SSS is currently limited to 47°S-47°N as we could not define unbiased SMOS reference dwell lines poleward of this latitude. This is likely because of imperfect correction for surface roughness and ice contamination which can extend up to 1000 km from the ice edge and which is much more difficult to mitigate than land-sea contamination as the ice edge is moving. Future studies should focus at correcting the ice contamination and improving roughness correction. In addition, in regions contaminated with highly variable RFI over the 7-year period, such as the northernmost parts of the Atlantic and Pacific Oceans, the land-sea contamination correction becomes very tricky. In our study, RFI affected Tbs are filtered out using a three-sigma filtering applied on SMOS Tbs before retrieving SSS and using a Chi filtering applied on L2 SSS. Future studies should look at improving this filtering.

7. Acknowledgements

We thank Stéphane Tarot for his very reactive support at CATDS CPDC. This work was supported by CNES-CATDS and CNES-TOSCA SMOS-Ocean projects. SMOS CATDS CEC data (also named L3_DEBIAS_LOCEAN_v2) have been produced by LOCEAN/IPSL (UMR CNRS/UPMC/IRD/MNHN) laboratory and ACRI-st company. CATDS-CPDC data (freely available at the CATDS) were operated for the "Centre National d'Etudes Spatiales" (CNES, France) by IFREMER (Brest, France). Both products are available at www.catds.fr.

SMAP CAP SSS is produced at Jet Propulsion Laboratory. It is available on ftp://podaac-ftp.jpl.nasa.gov/allData/smap/. ISAS 13 analysis fields are made freely available by Laboratoire d'Océanographie Physique et Spatiale (LOPS) (http://www.umr-lops.fr/SNO-Argo/Products/ISAS-T-S-fields). Near real time ISAS analysis are produced by the Coriolis data center and are freely available via CMEMS web site CMEMS-Copernicus Services: http://marine.copernicus.eu/. SSS data derived from thermosalinograph instruments installed onboard voluntary observing ships were collected, validated, archived, and made freely available by the French Sea Surface Salinity Observation Service (http://www.legos.obs-mip.fr/observations/sss/). We thank anonymous reviewers for their comments which helped to improve the manuscript.

REFERENCES

Akhil, V. P., M. Lengaigne, F. Durand, J. Vialard, A. V. S. Chaitanya, M. G. Keerthi, V. V. Gopalakrishna, J. Boutin, and C. de Boyer Montégut (2016), Assessment of seasonal and year-to-year surface salinity signals retrieved from SMOS and Aquarius missions in the Bay of Bengal, *International Journal of Remote Sensing*, 37(5), 1089-1114, doi:10.1080/01431161.2016.1145362.

Alory G., T. Delcroix, P. Téchiné, D. Diverrès, D. Varillon, S. Cravatte, Y. Gouriou, J. Grelet, S. Jacquin, E. Kestenare, C. Maes, R. Morrow, J. Perrier, G. Reverdin, and F. Roubaud (2015), The French contribution to the Voluntary Observing Ships network of Sea Surface Salinity. *Deep Sea Res.*, 105, 1-18, doi:10.1016/j.DSR.2015.08.005.

E. Anterrieu, M. Suess, F. Cabot, P. Spurgeon and A. Khazâal (2015), An Additive Mask Correction Approach for Reducing the Systematic Floor Error in Imaging Radiometry by Aperture Synthesis," in *IEEE Geoscience and Remote Sensing Letters*, vol. 12, no. 7, pp. 1441-1445, doi: 10.1109/LGRS.2015.2406912.

Arias, M. and SMOS-Ocean Expert Support Laboratories, 2016, L2OS v622 Reprocessing Report, SO-RP-ARG-GS-0100 Issue:2, 29 February 2016, available on https://smos.argans.co.uk/docs/technotes/SO-RP-ARG-GS-0100_L2OS_Reprocessing_Report_v2.0_160229.pdf.

Boutin J., Vergely J.L., Marchand S. (2017). SMOS SSS L3 debias v2 maps generated by CATDS CEC LOCEAN. http://doi.org/10.17882/52804.

951 Bretherton, F.P., R.E. Davis and C.B. Fandry (1976) Technique for Objective Analysis and
952 Design of Oceanographic Experiments Applied to Mode-73. Deep-Sea Research. 23:559-582.

953 Brodzik, M. J., B. Billingsley, T. Haran, B. Raup, M. H. Savoie (2012) EASE-Grid 2.0:
954 Incremental but Significant Improvements for Earth-Gridded Data Sets. ISPRS International
955 Journal of Geo-Information, 1(1):32-45, doi:10.3390/ijgi1010032.

956 CATDS (2017a). CATDS-PDC L3OS 2P - Daily valid ocean salinity values product from
957 SMOS satellite. CATDS (CNES, IFREMER, LOCEAN). http://doi.org/10.12770/77edd308-
958 4296-4774-b6f3-5b38301cee18.

959 CATDS (2017b). CATDS-PDC L3OS 3P mixed - Average 10 days & monthly salinity field
960 product from SMOS satellite (mixed orbits). CATDS (CNES, IFREMER, LOCEAN).
961 http://doi.org/10.12770/75ccd428-74b5-45db-879e-37ab98fa28a1

962 CATDS (2017c). CATDS-PDC L3OS 3Q mixed - Debiased average 10 days & monthly
963 salinity field product from SMOS satellite (mixed orbits). CATDS (CNES, IFREMER,
964 LOCEAN, ACRI). http://doi.org/10.12770/0f02fc28-cb86-4c44-89f3-ee7df6177e7b

965 Chaittanya, A.V.S., M. Lengaigne, J. Vialard, V.V. Gopalakrishna, F. Durand, Ch.
966 Krantikumar, V. Suneel, F. Papa and M. Ravichandran (2014), Fishermen-operated salinity
967 measurements reveal a “river in the sea” flowing along the east coast of India, Bull. Am. Met.
968 Soc., 95, 1897-1908.

969 Delcroix, T., M. McPhaden, A. Dessier, and Y. Gouriou (2005), Time and space scales for
970 sea surface salinity in the tropical oceans. *Deep Sea. Res.*, 52/5, 787-813,
971 doi:10.1016/j.dsr.2004.11.012.

972 Durack, P. J., Wijffels, S. E., and Matear, R. J. (2012), Ocean salinities reveal strong global
973 water cycle intensification during 1950 to 2000. *Science*, *336*(6080), 455-458.

974 Font, J., A. Camps, A. Borges, M. Martin-Neira, J. Boutin, N. Reul, Y. H. Kerr, A. Hahne,
975 and S. Mecklenburg (2010), SMOS: The Challenging Sea Surface Salinity Measurement
976 From Space, *Proceedings of the IEEE*, *98*(5), 649-665.

977 Fore, A. G., S. H. Yueh, W. Tang, B. W. Stiles, and A. K. Hayashi (2016a), Combined
978 active/passive retrievals of ocean vector wind and sea surface salinity with SMAP. *IEEE*
979 *Trans. Geosci. Remote Sens.*, 54(12):7396-7404, December 2016.

980 Fore, A., S. Yueh, W. Tang, and A. Hayashi, (2016b), SMAP Salinity and Wind Speed Data
981 User's Guide Version 3.0, JPL, 30 December 2016.

982 Fournier, S., J. T. Reager, T. Lee, J. Vazquez-Cuervo, C. H. David, and M. M. Gierach
983 (2016), SMAP observes flooding from land to sea: The Texas event of 2015, *Geophys. Res.*
984 *Lett.*, 43, 10,338–10,346, doi:10.1002/2016GL070821.

985 Fournier, S., Vialard, J., Lengaigne, M., Lee, T., Gierach, M. M., & Chaitanya, A. V. S.
986 (2017), Modulation of the Ganges-Brahmaputra river plume by the Indian Ocean dipole and
987 eddies inferred from satellite observations. Journal of Geophysical Research: Oceans, 122,
988 9591–9604. https://doi.org/10.1002/2017JC013333.

989 Gaillard F. (2015), ISAS-13 temperature and salinity gridded fields. SEANOE.
990 http://doi.org/10.17882/45945.

991 Gaillard, F., T. Reynaud, V. Thierry, N. Kolodziejczyk and K. von Schuckmann (2016), *In*
992 *situ*–Based Reanalysis of the Global Ocean Temperature and Salinity with ISAS: Variability
993 of the Heat Content and Steric Height, *J. Clim.*, 29, 1305-1323, doi:10.1175/JCLI-D-15-
994 0028.1.

995 Grodsky, S. A., N. Reul, B. Chapron, J. A. Carton, and F. O. Bryan (2017), Interannual
996 surface salinity on Northwest Atlantic shelf, *J. Geophys. Res. Oceans*, 122, 3638–3659,
997 doi:10.1002/2016JC012580.

998 Hasson, A., T. Delcroix, J. Boutin, R. Dussin, and J. Ballabrera-Poy (2014), Analyzing the
999 2010–2011 La Niña signature in the tropical Pacific sea surface salinity using *in situ* data,
1000 SMOS observations, and a numerical simulation, *Journal of Geophysical Research: Oceans*,
1001 119(6), 3855-3867, doi:10.1002/2013JC009388.

1002 Hasson, A., M. Puy, J. Boutin, E. Guilyardi (2018), Northward Propagation across the
1003 Tropical North Pacific Ocean Revealed by Surface Salinity: How El Nino Anomalies Reach
1004 Hawaii?, *Journal of Geophys. Res., in revision*.

1005 Hernandez, O., Boutin, J., Kolodziejczyk, N., Reverdin, G., Martin, N., Gaillard, F., Reul, N.,
1006 & Vergely, J.L. (2014). SMOS salinity in the subtropical North Atlantic salinity maximum: 1.
1007 Comparison with Aquarius and *in situ* salinity. *Journal of Geophysical Research: Oceans*,
1008 119, 8878-8896.

1009 Kerr, Y. H., et al. (2010), The SMOS Mission: New Tool for Monitoring Key Elements of the
1010 Global Water Cycle, *Proceedings of the IEEE*, *98*(5), 666-687.

1011 Kolodziejczyk, N., O. Hernandez, J. Boutin, and G. Reverdin (2015a), SMOS salinity in the
1012 subtropical North Atlantic salinity maximum: 2. Two-dimensional horizontal thermohaline
1013 variability, *J. Geophys. Res. Oceans*, 120, 972–987, doi:10.1002/2014JC010103.

1014 Kolodziejczyk, N., G. Reverdin, J. Boutin, and O. Hernandez (2015b), Observation of the
1015 surface horizontal thermohaline variability at mesoscale to submesoscale in the north-eastern
1016 subtropical Atlantic Ocean, *Journal of Geophysical Research: Oceans*, 120(4), 2588-2600,
1017 doi:10.1002/2014JC010455.

1018 Kolodziejczyk, N., J. Boutin, J.L. Vergely, S. Marchand, N. Martin, and G. Reverdin (2016).
1019 Mitigation of systematic errors in SMOS sea surface salinity. *Remote Sensing of*
1020 *Environment, 180*, 164-177.

1021 Lagerloef, G., et al. (2008), The Aquarius/SAC-D mission: Designed to meet the salinity
1022 remote sensing challenge *Oceanography*, *21*(1), 68–81.

1023 Lagerloef, G. (2012), Satellite mission monitors ocean surface salinity, *Eos Transactions of*
1024 *the AGU*, **93**(25), 233-234.

1025 Meissner, T. and F. J. Wentz (2016), Remote Sensing Systems SMAP Ocean Surface
1026 Salinities [Level 2C, Level 3 Running 8-day, Level 3 Monthly], Version 2.0 validated
1027 release. Remote Sensing Systems, Santa Rosa, CA, USA. Available online at
1028 www.remss.com/missions/smap, doi: 10.5067/SMP20-3SPCS.

1029 Mohammed, P. N. , M. Aksoy J. R. Piepmeier J. T. Johnson A. Bringer (2016), SMAP L-
1030 band microwave radiometer: RFI mitigation prelaunch analysis and first year on-orbit
1031 observations, *IEEE Trans. Geosci. Remote Sens.*, vol. 54 no. 10 pp. 6035-6047.

Oliva, R., Daganzo-Eusebio, E., Kerr, Y., Mecklenburg, S., Nieto, S., Richaume, P., Gruhier, C. (2012), SMOS Radio frequency interference scenario: status and actions taken to improve the RFI environment in the 1400–1427-MHz passive band. *IEEE Trans. Geosci. Remote Sens.* 50 (5), 1427–1440.

Olmedo, E., Martínez, J., Turiel, A., Ballabrera-Poy, J., & Portabella, M. (2017), Debiased non-Bayesian retrieval: A novel approach to SMOS Sea Surface Salinity. *Remote Sensing of Environment, 193*, 103-126.

Picaut, J., M. Ioualalen, T. Delcroix, F. Masia, R. Murtugudde, and J. Vialard (2001), The oceanic zone of convergence on the eastern edge of the Pacific warm pool: A synthesis of results and implications for ENSO and biogeochemical phenomena, J. Geophys. Res., 106, 2363–2386.

Piepmeier J. R. *et al*., (2017), SMAP L-Band Microwave Radiometer: Instrument Design and First Year on Orbit," in *IEEE Transactions on Geoscience and Remote Sensing*, vol. 55, no. 4, pp. 1954-1966, doi: 10.1109/TGRS.2016.2631978.

Reul N., and Coauthors (2014a), Sea Surface Salinity Observations from Space with the SMOS Satellite: A New Means to Monitor the Marine Branch of the Water Cycle. *Surveys In Geophysics*, **35(**3), 681-722.

Reul, N., B. Chapron, T. Lee, C. Donlon, J. Boutin, and G. Alory (2014b), Sea surface salinity structure of the meandering Gulf Stream revealed by SMOS sensor, Geophysical Research Letters, 41(9), 3141-3148, doi:10.1002/2014gl059215.

Shenoi, S. S. C., D. Shankar (2002), Differences in heat budgets of the near-surface Arabian Sea and Bay of Bengal: Implications for the summer monsoon, J. Geophys. Res., 107(C6), doi:10.1029/2000JC000679,.

SMOS-Ocean Expert Support Laboratories (2014), SMOS L2 OS Algorithm Theoretical Baseline Document, SO-TN-ARG-GS-0007, available on https://smos.argans.co.uk/docs/deliverables/delivered/ATBD/SO-TN-ARG-GS-0007_L2OS-ATBD_v3.11_140905.pdf.

Sommer, A., Reverdin, G., Kolodziejczyk, N., and Boutin, J. (2015), Sea Surface Salinity and Temperature Budgets in the North Atlantic Subtropical Gyre during SPURS Experiment: August 2012-August 2013. Frontiers in Marine Science, 2, 107.

Spurgeon and SMOS-Ocean Expert Support Laboratories (2017), L2OS v662 Reprocessing Report, SO-RP-ARG-GS-0109, available on https://earth.esa.int/documents/10174/477987/SMOS-Level-2-Ocean-Salinity-v662-Reprocessing-Report/3587ea20-45d1-49a5-a6ca-084d1bf988b6?version=1.4.

Supply, A., J. Boutin, J.-L. Vergely, N. Martin, A. Hasson, G. Reverdin, C. Mallet, N. Viltard (2017), Precipitation Estimates from SMOS Sea Surface Salinity, QJRMS, doi:10.1002/qj.3110.

Tang, W., A. Fore, S. Yueh, T. Lee, A. Hayashi, A. Sanchez-Franks, B. King, D. Baranowski, and J. Martinez (2017), Validating SMAP SSS with in-situ measurements. Remote Sensing Environ.. https://doi.org/10.1016/j.rse.2017.08.021.

Vergely and Boutin (2017), SMOS OS level 3: the Algorithm Theoretical Basis Document (v300), 05/05/2017, available on http://www.catds.fr/content/download/78841/1005020/file/ATBD_L3OS_v3.0.pdf?version=3 .

Vialard, J. and P. Delecluse (1998), An OGCM Study for the TOGA Decade. Part I : Role of Salinity in the Physics of the Western Pacific Fresh Pool. Journal of Physical Oceanography, 28, 1071 - 1088.

Yin, X., Boutin, J., & Spurgeon, P. (2012). First assessment of SMOS data over open ocean: Part I; Pacific Ocean. IEEE Transactions on Geoscience and Remote Sensing, 50(5), 1648–1661.

Yin, X., J. Boutin, P. Spurgeon, Biases Between Measured and Simulated SMOS Brightness Temperatures Over Ocean: Influence of Sun (2013), IEEE Journal of Selected Topics in Applied Earth Observations and Remote Sensing, doi: 10.1109/JSTARS.2013.2252602.

Zine, S., J. Boutin, J. Font, N. Reul, P. Waldteufel, C. Gabarró, J. Tenerelli, F. Petitcolin, J. L. Vergely, M. Talone, and S. Delwart (2008), Overview of the SMOS sea surface salinity prototype processor, *IEEE T. Geosci. Remote Sensing*, *46*, 621-645.

List of Figure Captions:

Figure 1 : Satellite SSS: SMOS SSS corrected according to (a, d, g, j) K2016 methodology, (b, e, h, k) the method described in this paper (CEC); (c, f, i, l) SMAP SSS. 4 case study areas : (a, b, c) : Bay of Bengal - August 21st 2015; (d, e, f) : Gulf of Mexico – August18th 2015 ; (g, h, i) : Eastern Tropical Atlantic Freshwater Pools – April 14th 2016; (j, k, l) : Amazon plume – October 21st 2015. SMOS and SMAP SSS are averaged over respectively a SMOS repetitive orbit sub-cycle (18 days) and two SMAP repetitive orbit cycles (16 days). Striking fresh SSS features in better agreement with SMOS (new version) and SMAP are indicated with black arrows.

Figure 2: Two examples of 2011-2016 latitudinal profiles of mean SSS (a; b) and of the standard deviation of the 2011-2016 monthly differences between SMOS SSS and ISAS SSS (c; d). The latitudinal means and standard deviations are computed over the Pacific Ocean

further than 1200 km from any coast: green: ISAS, blue: SMOS ascending orbits; red: SMOS descending orbits: a;c) November; middle of the swath (0-50 km from the center of the swath); b; d) January; edge of the swath (350-400 km from the center of the swath). Dashed vertical lines indicate 47°N and 47°S.

Figure 3: a) SSS variability (σ_{SSSnat}) derived from 7 years of SMOS filtered and corrected SSS (after debiasing and filtering): large values are observed in river plumes and in rainy areas (ITCZ, SPCZ. b) Minimum and c) maximum of the SSS as derived from 18-day CEC LOCEAN that are used in the mapping of debiased near-real time products (see section 3.4).

Figure 4: Monthly SMOS SSS compared to monthly ISAS SSS from July 2010 to December 2016. Standard deviation of the differences for a) L3P SMOS SSS; b) L3Q SMOS SSS. c) Number of months with differences between L3P and L3Q SMOS SSS greater than 0.2pss. d) Frequency with which corrections identified on Figure c) correspond to decreased bias with respect to ISAS (i.e. L3Q SMOS SSS closer to ISAS SSS than L3P SMOS SSS): red color means that the correction improves most of the time; blue color means that the correction degrades most of the time. Blank colors in figures c) and d) mean no change above the 0.2 pss threshold or no data in the L3P version (the comparison is done only for valid L3P SSS).

Figure 5: Comparison of SMOS and SMAP 'weekly' SSS: (a, d, g) r^2, (b, e, h) standard deviation of the differences, (c, f, i) number of pixels used in the comparisons. (a, b, c) 10-day L3P SMOS SSS, (d, e, f) 10-day L3Q SMOS SSS, (g, h, i) 9-day CEC SMOS SSS. Same indicators but when considering only the pixels available in the four products are presented in Appendix A2.

Figure 6: Scatter plots of SMOS corrected fields versus SMAP SSS on the 4 regions and fresh events periods illustrated on Figure 1: first line: Bay of Bengal; 2nd line: Gulf of Mexico; 3rd line : Eastern Tropical Atlantic Freshwater Pools; 4th line : Amazon plume. First

column: SMOS K2016 SSS; second column: SMOS 18-day CEC SSS; last column: SMOS 9-day CEC SSS.

Figure 7: Time series of statistical parameters computed over the Bay of Bengal case study area, April 2015 to December 2016: a) mean SSS; b) SSS standard deviation; c) square of the Pearson correlation coefficient (r^2) between SMOS and SMAP SSS; d) Standard deviation of the SMOS minus SMAP SSS differences (plain line) using L1 norm (dotted line). 'Weekly' SMOS CEC(blue), 'bi-weekly' SMOS CEC (green), 'bi-weekly' SMOS K2016 (red), 'weekly' SMAP (black).

Figure 8: Time series of statistical parameters computed over the Gulf of Mexico case study area, April 2015 to December 2016: a) mean SSS; b) SSS standard deviation; c) square of the Pearson correlation coefficient (r2) between SMOS and SMAP SSS; d) Standard deviation of the SMOS minus SMAP SSS differences (plain line) using L1 norm (dotted line). 'Weekly' SMOS CEC(blue), 'bi-weekly' SMOS CEC (green), 'bi-weekly' SMOS K2016 (red), 'weekly' SMAP (black).

Figure 9: Time series of statistical parameters computed over the Eastern Tropical Atlantic Freshwater Pools case study area, April 2015 to December 2016: a) mean SSS; b) SSS standard deviation; c) square of the Pearson correlation coefficient (r2) between SMOS and SMAP SSS; d) Standard deviation of the SMOS minus SMAP SSS differences (plain line) using L1 norm (dotted line). 'Weekly' SMOS CEC(blue), 'bi-weekly' SMOS CEC (green), 'bi-weekly' SMOS K2016 (red), 'weekly' SMAP (black).

Figure 10: Time series of statistical parameters over the Amazon plume case study area, April 2015 to December 2016: a) mean SSS; b) SSS standard deviation; c) square of the Pearson correlation coefficient (r2) between SMOS and SMAP SSS; d) Standard deviation of the SMOS minus SMAP SSS differences (plain line) using L1 norm (dotted line). 'Weekly' SMOS CEC(blue), 'bi-weekly' SMOS CEC (green), 'bi-weekly' SMOS K2016 (red), 'weekly' SMAP (black).

Figure 11: Top: Density spectra; Bottom: Coherence between ship SSS and SMOS or ISAS SSS. The spatial frequency (1/wavelength (km)) is indicated below the bottom plot, whereas the corresponding wavelengths (km) are indicated above the top plot. Vertical dashed lines correspond to spatial frequencies regularly spaced in logarithmic coordinates. Northern subtropical Atlantic (see box on the color map) in 2013. Ship SSS measured on regular merchant ships transects (14 regular transects in 2013) (black), ISAS SSS (green), 10-day SMOS L3P (blue line), 10-day SMOS L3Q (dashed blue line), 18-day SMOS CEC (red line), 9-day SMOS CEC (red dashed line).

Figure 12: Statistics of ship comparisons (May 2010-August 2016) binned as a function of the distance from the nearest coast: top) mean difference; middle) standard deviation of the differences; the black line indicates the standard deviation of ship SSS in each class; bottom) number of pixels used in the comparisons. Left: considering only the SMOS pixels common to all versions; right: considering all pixels available in each version. Ship and SMOS SSS are integrated over 100 km. Orange: monthly SMOS L3P ; pink : monthly SMOS L3Q; light blue : 18-day SMOS CEC; green : ISAS.

Figure 13: Examples of comparisons between ship SSS (black stars line) and SMOS SSS: orange: non corrected (L3P), purple: monthly L3Q corrected, light blue :18-day CEC corrected; green : ISAS. Left) from 2014-08-21 to 2014-09-03, Matisse ship. Right) from 2013-08-21 to 2013-09-03, Santa Cruz ship. All SSS products have been smoothed over +/-50 km.

Figure 14: Standard deviation of ‘weekly’ satellite SSS minus ISAS SSS between 47°N and 47°S, over the year 2016. a) SMOS CEC, b) SMAP CAP.

Figure 15: SSS latitudinal profiles in December 2011(top left), 2012 (top right), 2013 (bottom left), 2014 (bottom right) in the Atlantic Ocean (1200 km from continents)- SMOS ascending orbits (blue), descending orbits (red), ISAS(green).

Figure 16: SSS latitudinal profiles in December 2011(top left), 2012 (top right), 2013 (bottom left), 2014 (bottom right) in the Pacific Ocean (1200 km from continents)- SMOS ascending orbits (blue), descending orbits (red), ISAS(green).

Figure 17: Median of SMOS minus ISAS SSS absolute differences as a function of dwell line location and year, for the month of January (left), May (middle) and September (right), for ascending (top) and descending (bottom) orbits. The black lines indicate the range of selected x_{swath}.

Figure 18: 'Weekly' comparison of SMOS and SMAP SSS: (a, c, e) square of the Pearson correlation coefficient (r^2) , (b, d, f) standard deviation of the difference. (a, b) L3P SMOS SSS, (c, d) L3Q SMOS SSS, (e, f) CEC SMOS SSS. Only pixels common to the four products are considered in the comparisons.

Appendix A1: Selection of the region and of the reference x_{swath} to be used for the seasonal latitudinal correction:

Given the high RFI contamination in the northern latitudes of the Atlantic Ocean and given the relatively small area further than 1000 km from the continents in the Atlantic Ocean, we choose to estimate the seasonally-varying latitudinal biases from Pacific Ocean orbits only. Nevertheless, before doing this choice, we checked, on x_{swath} and periods not very affected by RFI at high latitudes, that biases are similar in the Pacific and Atlantic Ocean. We observe that the differences between ocean basins are on the same order of magnitude as the interannual variability of the biases as illustrated with a few examples on Figure 15 and on Figure 16.

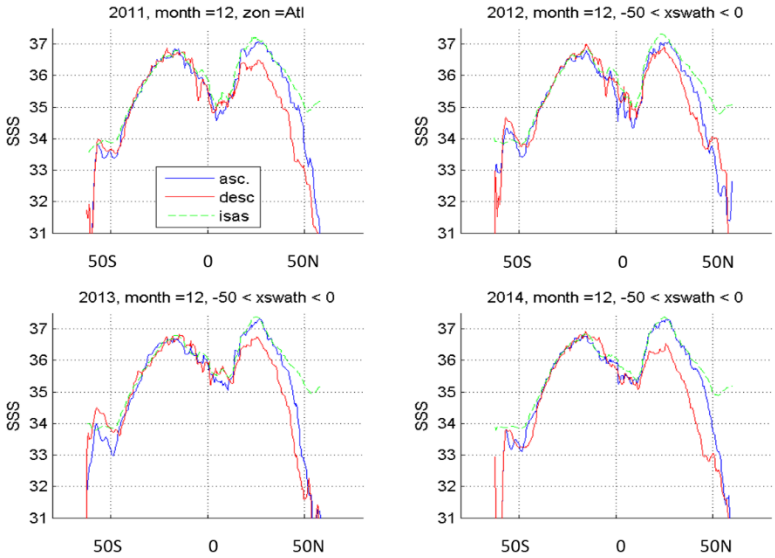

Figure 15: SSS latitudinal profiles in December 2011(top left), 2012 (top right), 2013 (bottom left), 2014 (bottom right) in the Atlantic Ocean (1200 km from continents)- SMOS ascending orbits (blue), descending orbits (red), ISAS(green).

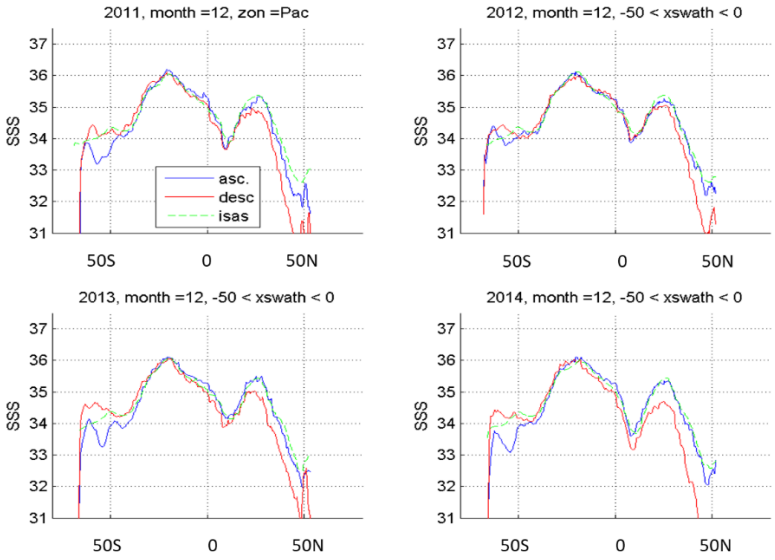

Figure 16: SSS latitudinal profiles in December 2011(top left), 2012 (top right), 2013 (bottom left), 2014 (bottom right) in the Pacific Ocean (1200 km from continents)- SMOS ascending orbits (blue), descending orbits (red), ISAS(green).

Over the 2011-2016 period, for each x_{swath}, each month and each x_{orb}, reference x_{swath} are chosen as the ones having relatively weak and stable (from one year to another) SMOS minus ISAS SSS differences (DIFF) over the 45°S-45°N latitudinal range. We did not define a

quantitative criterion for this selection because the patterns of DIFF strongly vary from one month to another, from ascending to descending orbits and as a function of latitude (not shown). During most months, reference x_{swath} are located on ascending orbits only. We illustrate the location of the reference x_{swath} with respect to the median of SMOS minus ISAS SSS absolute differences for the months of January, May and September (Figure 17). The locations of all the selected reference x_{swath} are reported in Table 4.

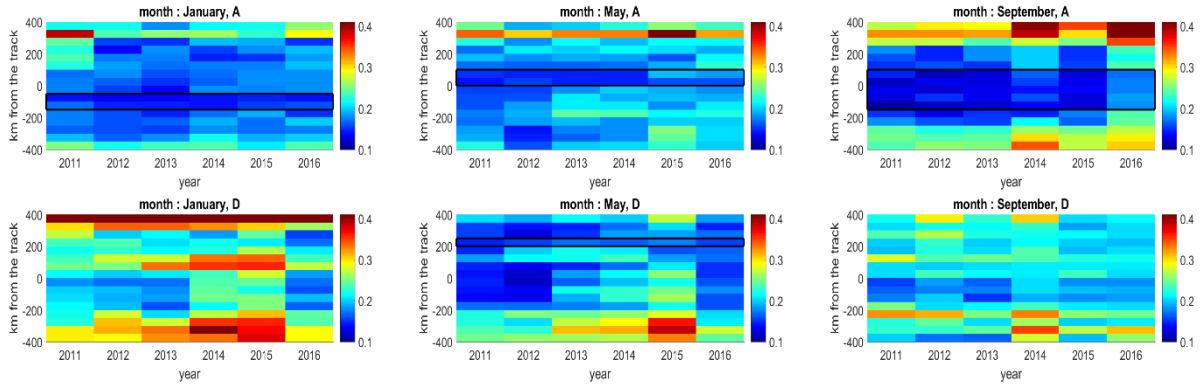

Figure 17: Median of SMOS minus ISAS SSS absolute differences as a function of dwell line location and year, for the month of January (left), May (middle) and September (right), for ascending (top) and descending (bottom) orbits. The black lines indicate the range of selected x_{swath}.

Table 4: Reference x_{swath} locations

	Ascending orbits	Descending orbits
January	[-150 -50] km	-
February	[-250 -100] km	-
March	[-250 -100] km	-
April	[0 100] km	[150 200] km
May	[0 100] km	[200 250] km
June	[50 100] km	[50 100] km

July	[-150 50] km	[50 100] km
August	[-250 250] km	[-50 100] km
September	[-150 100] km	-
October	[-50 100] km	-
November	[-250 -100] km	-
December	[-100 -50] km	-

1218

1219

1220 **Appendix A2: SMOS-SMAP SSS comparison considering only pixels common**

1221 **to all SSS fields:**

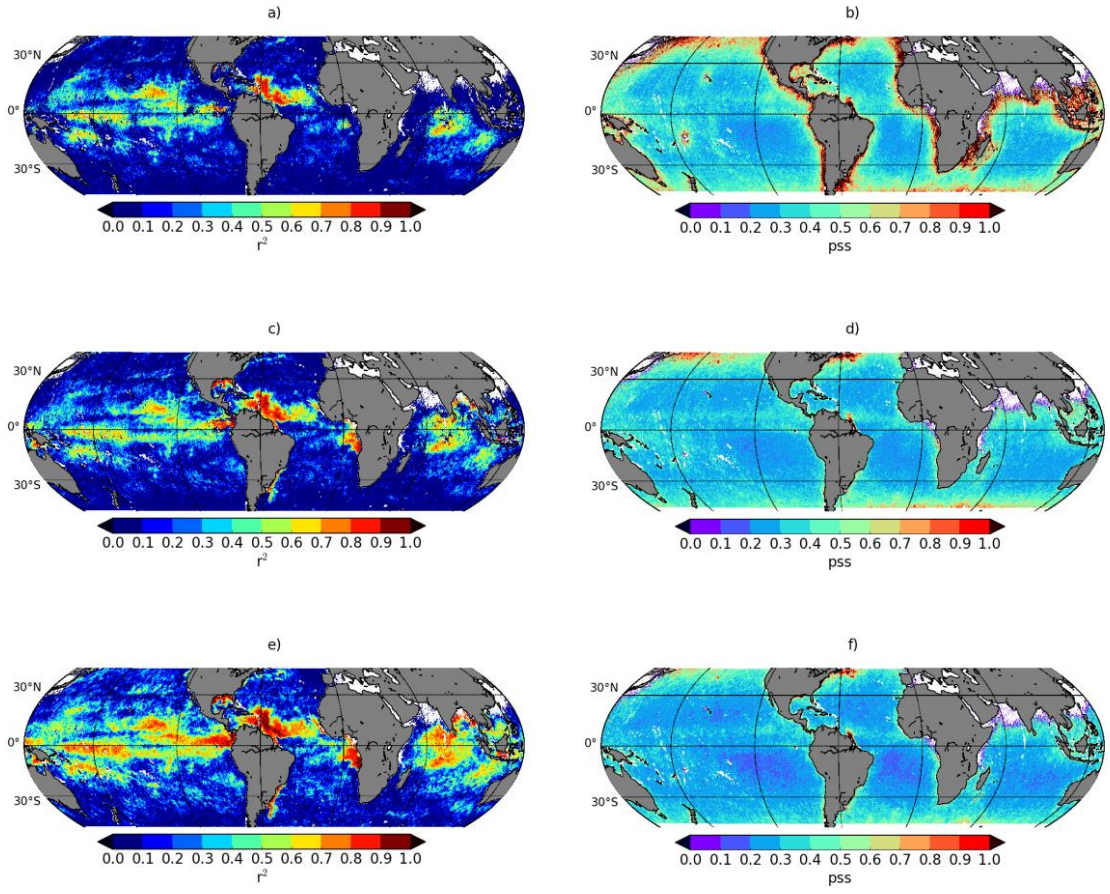

Figure 18: ‘Weekly’ comparison of SMOS and SMAP SSS: (a, c, e) square of the Pearson correlation coefficient (r^2) , (b, d, f) standard deviation of the difference. (a, b) L3P SMOS SSS, (c, d) L3Q SMOS SSS, (e, f) CEC SMOS SSS. Only pixels common to the four products are considered in the comparisons.